Distal Pb-Zn-Ag veins associated with the world-class Donggou porphyry Mo deposit, southern North China craton

Zhan-Ke Li[1], Shi-Jian Bi[1], Jian-Wei Li[1, 2*], Wen Zhang[2], David R. Cooke[3], David Selby[4]

1. Faculty of Earth Resources, China University of Geosciences, Wuhan, Hubei Province 430074, China

2. State Key Laboratory of Geological Processes and Mineral Resources, China University of Geosciences, Wuhan, Hubei Province 430074, China

3. Transforming the Mining Value Chain, CODES, University of Tasmania, Private Bag 79, Hobart, Tasmania, 7001, Australia

4. Department of Earth Sciences, University of Durham, Durham DH1 3LE, United Kingdom

† **Corresponding author:**

E-mail: jwli@cug.edu.cn

Ph: 00 86 138 71112076

Fax: 00 86 27 67885099

Abstract

The southern North China craton hosts numerous world-class porphyry Mo and Pb-Zn-Ag vein deposits. Whether or not the Pb-Zn-Ag veins are genetically associated with the porphyry Mo system remains contentious. Here we focus on the genetic relationships between the Sanyuangou Pb-Zn-Ag vein deposit and the world-class Donggou porphyry Mo deposit, and discuss the potential implications from the spatial and temporal relationships between porphyry and vein systems in the southern North China craton.

At Sanyuangou, vein-hosted sulfide mineralization mainly comprises pyrite, sphalerite, and galena, with minor chalcopyrite, pyrrhotite, bornite, tetrahedrite, covellite, polybasite and argentite. The mineralization is hosted by a quartz diorite stock, which has a zircon U-Pb age of 1756 ± 9 Ma. However, sericite from alteration selvages of Pb-Zn-Ag sulfide mineralization yields a well-defined $^{40}Ar/^{39}Ar$ plateau age of 115.9 ± 0.9 Ma. Although nominally younger, the sericite $^{40}Ar/^{39}Ar$ age is similar to the age of the nearby Donggou porphyry Mo deposit (zircon U-Pb age of 117.8 ± 0.9; molybdenite Re-Os ages of 117.5 ± 0.8 Ma and 116.4 ± 0.6 Ma). Pyrite from Donggou has elevated contents of Mo and Bi, whereas pyrite from Sanyuangou is enriched in Cu, Zn, Pb, Ag, Au, and As. This trace element pattern is consistent with metal zonation typically observed in porphyry related metallogenic systems. Pyrite grains from Sanyuangou have lead isotopes overlapping those from Donggou (17.273-17.495 vs. 17.328-17.517 for $^{206}Pb/^{204}Pb$, 15.431-15.566 vs. 15.408-15.551 for $^{207}Pb/^{204}Pb$, and 37.991-38.337 vs. 38.080-38.436 for $^{208}Pb/^{204}Pb$). Collectively, the geological, geochronological, and geochemical data support a magmatic-hydrothermal origin for the Sanyuangou Pb-Zn-Ag deposit and confirm that the Pb-Zn-Ag veins and the Donggou Mo deposit form a porphyry-related magmatic-hydrothermal system.

Given the widespread Pb-Zn-Ag veins and Mo mineralized porphyries in many districts of the southern North China craton, the model derived from this study has broad implications for further exploration of Mo and Pb-Zn-Ag resources in the area.

Key words: porphyry Mo deposit; Pb-Zn-Ag veins; geochronology; trace elements; *in-situ* lead isotopes; Donggou deposit

Introduction

Porphyry deposits are the world's most important repositories of Cu and Mo (Sillitoe, 2000). They are commonly generated above subduction zones at convergent margins and are associated with contemporaneous calc-alkaline magmas (Richards 2003; Cooke et al., 2005; Seedorff et al., 2005). Some deposits, especially porphyry Mo deposits in continental collision setting, are associated with high K calc-alkaline to shoshonite magmas (e.g., Chen et al., 2004, 2016; Li et al., 2007; Mao et al., 2010). Porphyry-related base metal vein and replacement mineralization may form economically important Zn, Pb, Cu, Ag, and Au deposits proximal or distal to porphyry Cu and Mo deposits (Lang and Eastoe, 1988; Sillitoe, 2010; Catchpole et al., 2015). A continuum of porphyry-related mineralization styles was proposed by Sillitoe (1973) to explain the close spatial relationship of various hydrothermal deposit types (porphyry, skarn, base and precious metal veins, and epithermal deposits) in many porphyry systems. Geochemical footprints of the porphyry system commonly comprise a district-scale metal zonation of Cu-Mo through Zn-Pb to Ag-Au (Emmons, 1927; Jones, 1992; Dilles and Einaudi, 1992; Babcock et al., 1995; Seedorff et al., 2005; Sillitoe, 2010). Such metal zonation, when properly recognized, may provide useful exploration vectors to end-member mineralization styles in a porphyry related metallogenic system. A comprehensive geochronological and geochemical study is critically important in constraining a possible genetic link between porphyry and peripheral Zn-Pb-Cu-Ag-Au mineralization (e.g., Lawley et al., 2010; Schütte et al., 2012; Catchpole et al., 2015).

Large areas of the southern North China craton (NCC) host several giant mineral concentrations (Fig. 1). The Xiaoqinling district has been China's second largest gold producer in the last three decades (Mao et al., 2002; Li et al., 2012a, 2012b). To the east, the Xiong'ershan district has traditionally been an important gold producer (Chen and Fu, 1992; Fan et al., 2000), but has also recently become the most important silver producer and a significant Zn-Pb source along the southern NCC (Chen et al., 2004; Mao et al., 2006; Li et al., 2010, 2013b). The Luonan-Lushi, Luanchuan and Waifangshan districts host several world-class porphyry Mo deposits (Fig. 1; Li et al., 2005; Ye et al., 2006; Mao et al., 2011). Molybdenite Re-Os dating has revealed two pulses of porphyry intrusion and porphyry-skarn Mo mineralization at 148-138 Ma and 131-112 Ma, respectively (Mao et al., 2008). These Mo deposits are unrelated to a convergent plate margin; rather they are located in intracontinental settings and are associated with high K calc-alkaline or alkaline felsic magmas induced

by thinning and destruction of lithosphere beneath this craton during the Late Jurassic to Early Cretaceous (Mao et al., 2008, 2010, 2011; Pirajno and Zhou, 2015).

In the last two decades, numerous Pb-Zn-Ag veins have been discovered in some of the Mo-mineralized districts, such as the Lengshuibeigou deposit in the Luanchuan ore field (Fig. 1; Yan, 2004; Qi et al., 2007; Wang et al., 2013). Genesis of these Pb-Zn-Ag veins is debated (e.g., Chen and Fu, 1992; Chen et al., 2004; Mao et al., 2006, 2011; Yao et al., 2008; Li et al., 2013b). Previous studies interpret the Pb-Zn-Ag veins to be a porphyry-related (Ye, 2006; Mao et al., 2006, 2009, 2011; Wang et al., 2013), or an orogenic-type system associated with the Triassic orogenic deformation involving the continental collision between the North China and Yangtze cratons (Chen et al., 2004; Qi et al., 2007; Yao et al., 2008).

The Fudian ore field in southern NCC (Fig. 1) hosts the giant Donggou porphyry Mo deposit and numerous Pb-Zn-Ag vein deposits including Sanyuangou, Laodaizhanggou, and Wangpingxigou (Fig. 2). Current geochronologies for the Donggou porphyry Mo deposit are non-conclusive based on a SHRIMP zircon U-Pb age of 112 ± 1 Ma for the Donggou porphyry and molybdenite Re-Os ages of 116.5 ± 1.7 to 114.1 ± 1.4 Ma for Mo-bearing quartz and K-feldspar veins (Ye et al., 2006; Mao et al., 2008). In addition to the Donggou porphyry, several large granitoid intrusions and a number of diorite dikes occur in the Fudian ore field (Fig. 2). Most Pb-Zn-Ag veins are in close proximity of or hosted by these intrusions (Fig. 2), but the genetic relationship to the magmatic events has not been determined. Alteration selvage sericite associated with a Pb-Zn-Ag vein of the Sanyuangou deposit (Fig. 2) has an $^{40}Ar/^{39}Ar$ plateau age of 110.1 ± 9.2 Ma (Ye, 2006), which is roughly consistent with a sphalerite Rb-Sr isochron age of 117 ± 27 Ma for the Wangpingxigou Pb-Zn-Ag deposit (Fig. 2; Yao et al., 2010). The large uncertainties of the $^{40}Ar/^{39}Ar$ and Rb-Sr ages for the Pb-Zn-Ag deposits and the discordance between the U-Pb and Re-Os ages for the Donggou porphyry Mo deposit necessitates further precise geochronological coupled with geochemical studies to evaluate a possible genetic link between porphyry Mo and vein Pb-Zn-Ag mineralization.

Here we firstly present a comparative geochronology study (U-Pb, Re-Os, and $^{40}Ar/^{39}Ar$) for the Donggou porphyry Mo deposit and the Sanyuangou Pb-Zn-Ag vein deposit to assess their temporal relationship. We further analyze trace elements of pyrite from both deposits using laser ablation ICP-MS to investigate any geochemical affiliation between the two systems. Lastly, we use *in-situ* lead isotopes of pyrite to evaluate any genetic link between the Pb-Zn-Ag and porphyry Mo systems.

Synthesis of existing geological and geochronological data provides a metallogenic model that may prove a useful exploration guide for porphyry Mo and Pb-Zn-Ag veins in the whole southern NCC.

Geologic setting

The Fudian ore field is located in the Waifangshan district of the southern NCC (Fig. 1). The NCC consists of the Western and Eastern Blocks that are separated by the Trans-North China Orogen (TNCO) formed during collision between the two blocks at ca. 1.85 Ga (Fig. 1). This collision resulted in the final amalgamation and stabilization of the craton (Zhao et al., 2001). The basement of the NCC is dominated by Archean to Paleoproterozoic high-grade metamorphic rocks that are variably overlain by Mesoproterozoic to Late Paleozoic unmetamorphosed marine sedimentary rocks (Zhao et al., 2000, and references therein). Although, the NCC behaved as a coherent, stable continental block from the Late Paleoproterozoic to the Late Paleozoic (Yang et al., 1986; Zhai, 2010), its margins were repeatedly affected by Late Paleozoic to Early Mesozoic subduction and orogenesis (Chen and Fu, 1992). During the Late Mesozoic, the NCC witnessed extensive magmatism (Wu et al., 2005; Mao et al., 2010), exhumation of numerous metamorphic core complexes (Fig. 1; Wang and Zhang, 1999; Zhang and Zheng, 1999; Shi et al., 2004), and development of intracontinental rift-basins (Ren et al., 2002). These tectonic signatures are interpreted to be a consequence of tectonic reactivation or lithospheric destruction of the eastern NCC, induced by the westerly subduction of the paleo-Pacific plate in Early Cretaceous (e.g., Zhu et al., 2012).

The southern NCC is dominated by the Late Archean to Early Paleoproterozoic Taihua and Xiong'er Groups (Fig. 1). The Taihua Group consists of amphibolite facies metamorphic rocks, mainly including amphibolite, felsic gneiss, khondalite, migmatite, and metasedimentary rocks intercalated with mafic to ultramafic rocks (Hu et al., 1988; Chen and Fu, 1992). The amphibolites have a whole-rock Sm-Nd isochron age of 2,542 ± 57 Ma (Zhou et al., 1998), whereas the felsic gneisses and khondalite series have zircon U-Pb ages of 2.6-2.3 and 2.2-2.18 Ga, respectively (Xu et al., 2009; Li et al., 2015). The Xiong'er Group is distributed widely in the Xiaoshan, Xiong'ershan, and Waifangshan districts. It is composed of volcanic rocks ranging in composition from basalt to rhyolite, but dominated by andesite, with minor intercalations of clastic rocks (Zhao et al., 2002; Peng et al., 2008). *In-situ* zircon U-Pb dating indicates that rocks of the Xiong'er Group mainly erupted between 1.8 and

1.75 Ga (Zhao et al., 2004; He et al., 2009; Zhao et al., 2009). Mesozoic and Cenozoic sedimentary rocks are locally present in the area (Fig. 1).

To the south, the southern NCC is separated from the North Qinling Terrane by the NW-oriented Luanchuan Fault (Fig. 1), which was generated during the Mesozoic continental collision between the Yangtze and North China cratons forming the Qinling Orogen (Dong et al., 2011). The Machaoying Fault is an important north-dipping regional structure in the southern NCC, extending for more than 200 km along an approximately easterly strike (Fig. 1). Interpretation of geophysical data indicates that the Machaoying Fault is a translithospheric structure (Hu et al., 1988). Secondary structures affiliated with the Machaoying Fault are well developed and have been important in the formation and distribution of polymetallic deposits in the area (Fig. 1; Chen and Fu, 1992; Yan et al., 2000; Ma et al., 2006).

Mesozoic granitoid intrusions are widespread in the southern NCC (Fig. 1). To the west of the Waifangshan district, the Wuzhangshan and Huashan plutons intruded intermediate to acidic rocks of the Xiong'er Group at 157 ± 1 Ma and 132 ± 2 Ma, respectively (Mao et al., 2010). To the south of the district, the Heyu pluton consists of biotite monzonite and granite porphyry formed by multiphase magmatism between 148 and 127 Ma (Gao et al., 2010b; Mao et al., 2010; Li et al., 2012c, 2013a). Adjacent to the Heyu intrusive complex, the Taishanmiao pluton consists of coarse- to medium-grained K-feldspar granite, fine- to medium-grained syenogranite, and fine-grained granite (Qi, 2014), which were emplaced episodically between 125 and 115 Ma (Ye et al., 2008; Qi, 2014; Gao et al., 2014). Compositionally, the Taishanmiao granites are classified as K-rich, aluminous to peraluminous granite and aluminous A-type granite (Ye et al., 2008). A number of Mo-mineralized porphyries occur over the Waifangshan district and adjacent areas (Fig. 1). These porphyries have been dated at 158 to 112 Ma using *in-situ* zircon U-Pb geochronology (Li et al., 2006; Mao et al., 2010).

Geology of the Fudian ore field

The Fudian ore field is located in the eastern portion of the Waifangshan district (Fig. 1), immediately to the northeast of the Taishanmiao intrusive complex (Fig. 2). The ore field is dominated by basaltic andesite, andesite, dacite and rhyolites of the Paleoproterozoic Xiong'er Group, which are locally covered by Cenozoic unconsolidated sediments (Fig. 2). Brittle faults are well developed in the

Fudian ore field (Fig. 2). The NW-striking Yangping-Wangping Fault (F1) and Jincun-Fudian Fault (F2) are the main structures in the district, extending for more than 20 to 30 km along strike and dipping 70°-80° to the southwest (Huang et al., 1992). Both faults are characterized by well-developed tectonic breccias and cataclasite with intensive sericitization, chloritization, and silicification. Numerous NE-striking faults displace and thus postdate the NW-striking structures (Fig. 2). There are also some minor E-striking faults, which either crosscut or are displaced by the NE- or NW-oriented faults. The E- and NE-striking faults are the major structural hosts of the Pb-Zn-Ag veins in the Fudian ore field (Fig. 2; Huang et al., 1992; Ma et al., 2006).

Several granitoid intrusions were emplaced into the volcanic rocks of the Xiong'er Group (Fig. 2). They are compositionally dominated by quartz diorite and quartz monzonite, with minor diorites (Fig. 2). The quartz monzonite at Wangpingxigou is enclosed by, rather than intrudes, volcanic rocks of the Xiong'er Group. It intruded the Taihua Group and then covered by the Xiong'er Group. Ages of these magmatic intrusions are undetermined, but a Mesoproterozoic age is speculated by local geologists (HBGMR, 1989). The Donggou granite porphyry is the only Mesozoic intrusion at Fudian, but large plutonic bodies of similar ages crop out to the south of the ore field (Figs. 1, 2). The Donggou porphyry has an exposure of 0.01 km^2 (Fig. 3), but drill holes have revealed that it has a minimum lateral dimension of 1550 m and a vertical extent of >850 m (Fig. 4; Ye et al., 2006). The porphyry has phenocrysts dominated by perthite and quartz that account for 10-15 vol. % of the rocks, whereas the matrix is composed principally of perthite (40-55 vol. %), quartz (20-30 vol. %), plagioclase (10-20 vol. %) and albite (5-15 vol. %) with minor biotite. The rocks are weakly peraluminous with high Si, K, and Ga/Al ratios, and are classified as aluminous A-type granites (Dai et al., 2009). Whole-rock Sr-Nd and zircon Hf isotope data indicate that the porphyry was derived from partial melting of ancient lower crust with minor input of mantle-derived mafic magmas (Dai et al., 2009). Regional gravity and aeromagnetic data indicate a deep-seated plutonic body beneath the Donggou porphyry, likely representing the northward extension of the Taishanmiao intrusion at depth (Ye et al., 2006).

Mineralization

Mineralization in the Fudian ore field is largely represented by the Donggou porphyry Mo deposit and several Pb-Zn-Ag vein deposits (Fig. 2). The Donggou Mo deposit was discovered in 1984 by the

No. 2 Team of Henan Bureau of Geology and Mineral Resources during a regional geological survey, and has proven reserves of 0.63 Mt Mo at an average grade of 0.11 wt % (Ye et al., 2006). Spatially associated with the Donggou deposit are several Pb-Zn-Ag vein deposits hosted by E- or NE-striking faults, as best illustrated by the Sanyuangou, Wangpingxigou, and Laodaizhanggou deposits (Fig. 2). The combined reserves of these deposits is 0.93 Mt Pb + Zn (Ye, 2006; Yao et al., 2008), whereas the quantity of the Ag reserve is not published.

Donggou porphyry Mo deposit

The Donggou porphyry Mo deposit (112°22′50″ E, 33°57′03″ N) is related to the Donggou porphyry, which intruded andesite and basaltic andesite of the Xiong'er Group. Unlike typical porphyry Cu-Mo deposits where the ores are commonly localized in porphyritic intrusions, Mo mineralization at Donggou is mostly hosted in the andesite of the Xiong'er Group up to 360 m from the intrusive contact of the Donggou porphyry (Figs. 4, 5a, 5c). The ores in the volcanic rocks account for ca. 98 % of the total reserves of the deposit (Ma et al., 2007). Minor Mo mineralization occur in the uppermost zone (<70 m) of the Donggou porphyry (Figs. 4, 5b, 6a). The deposit consists of 19 orebodies, individually 47 to 254 m thick. Molybdenum mineralization in the Paleoproterozoic volcanic rocks is largely controlled by abundant fractures in the rocks that provided high permeability for magmatic-derived, Mo-bearing hydrothermal fluids (Yang et al., 2011, 2015).

Molybdenum mineralization is dominated by stockwork veinlets and veins bearing molybdenite, with minor amounts of sulfide disseminations (pyrite, chalcopyrite, sphalerite, and galena; Figs. 5, 6b-c) both within the Donggou porphyry and the proximal Paleoproterozoic volcanic rocks. They are largely represented by fine-grained molybdenite disseminations (Fig. 5a), coarse-grained molybdenite aggregates (Fig. 5b), and K-feldspar – molybdenite veins (Fig. 5c-d) that are commonly overprinted by quartz – molybdenite veins (Fig. 5d). Polymetallic sulfide veins occur locally in the proximal volcanic rocks. These veins are typically 10 to 50 cm wide and cut hydrothermally altered and Mo-mineralized andesite (Fig. 5e-f). Pyrite, sphalerite, and galena are abundant in these veins, with minor molybdenite and chalcopyrite (Figs. 5e-f, 6d-f).

Hydrothermal alteration is well developed both in the Donggou porphyry and the proximal andesite. The dominated alteration types are potassic (Fig. 5b-d) and silicic alteration (Fig. 5d-f).

Potassic alteration is largely represented by K-feldspar, locally associated with minor biotite, and typically occurs as mm-to-cm-scale aggregates of K-feldspar (Figs. 5a-d). Silicic alteration occurs mainly in the wall rocks surrounding the porphyry, shown by quartz with various amounts of sulfide minerals (Figs. 5d-f). Molybdenite is present both in the potassic and silicic assemblages, occurring mainly as aggregates (Fig. 5b-d). Less extensive alteration formed sericite, chlorite, and carbonate aggregates or irregular veinlets. Based on field and petrographic observations, four paragenetic stages are recognized at Donggou (Fig. 7): stage D1 (D is short for Donggou) K-feldspar – molybdenite veins; stage D2 quartz – molybdenite veins; stage D3 quartz – polymetallic sulfide veins; and stage D4 quartz – calcite veins. Molybdenite mainly occurs during stages D1 and D2.

Sanyuangou Pb-Zn-Ag deposit

In the whole Fudian ore field, Pb-Zn-Ag vein deposits share common geological and mineralization features. To understand their temporal and spatial relationships with the Donggou porphyry, here we focus on the Sanyuangou Pb-Zn-Ag vein deposit. The Sanyuangou deposit (112°22′19″ E, 33°55′55″ N) is located on the southern edge of the Fudian ore field, about 3 km to the south of the Donggou porphyry Mo deposit (Fig. 2). Mineralization is hosted in a quartz diorite stock elongated easterly that has been cut by numerous NW-, NE-, and E-oriented faults (Fig. 2). The Pb-Zn-Ag mineralization is largely represented by Pb-Zn-sulfide veins, which mainly occur in E-striking faults (Figs. 2, 8a-b). These vein-hosting faults commonly dip 70°-85° to the north, but locally steeply dip to the south. Individual veins are usually 300 to 2,000 m long, 0.5 to 5 m wide, and continuous for several hundred meters down plunge. Quartz – pyrite veins are typically crosscut by Pb-Zn-sulfide veins (e.g., Fig. 8a). Individual Pb-Zn-ore shoots are separated by less mineralized, subeconomic segments along the veins (Fig. 8a-d). Massive sulfide ores (Fig. 8c-e) are common, and preferentially localized in dilational jogs, splays, and bifurcations along the structures. Sulfide minerals in the Pb-Zn-Ag veins are dominated by pyrite, sphalerite, and galena, with minor amounts of chalcopyrite, pyrrhotite, bornite, tetrahedrite, and covellite (Figs. 8a-e, 9a-d). Galena is the main silver-bearing mineral, but minor polybasite and argentite are also present.

Hydrothermal alteration is well developed and ranges from cm-wide selvages to meter-wide halos (e.g., Fig. 8a). The alteration assemblages consist mainly of quartz, sericite, siderite, ankerite, and

calcite, with minor chlorite (Figs. 8a, f, 9e-f). Field and textural relationships indicate three paragenetic stages (Fig. 10): stage S1 (S is short for Sanyuangou) quartz – pyrite veins; stage S2 quartz – polymetallic sulfide veins; and stage S3 quartz – calcite veins. Pb-Zn-Ag mineralization is mainly associated with stage S2.

Samples and Analytical Methods

Geochronology

Zircon U-Pb dating

The Donggou granite porphyry (DG01) hosting the Donggou porphyry Mo deposit and the quartz diorite (SY01) and quartz monzonite (WP01) hosting the Sanyuangou and Wangpingxigou Pb-Zn-Ag vein deposits, respectively, were collected for zircon U-Pb geochronology (Figs. 2, 3). U-Pb dating of quartz diorite and quartz monzonite was aimed to test previous speculations that these host rocks are temporarily and genetically related to the Pb-Zn-Ag mineralization. Zircon grains were handpicked under a binocular microscope after conventional crushing, liquid and magnetic separation. Representative grains were mounted in epoxy resin disks, and then polished, cleaned, and gold coated. Prior to isotopic analysis, all grains were photographed under transmitted- and reflected-light microscope and then imaged using the cathodoluminescence (CL) technique with a JEOL 8800 electron microprobe.

Zircon U-Pb dating was conducted using laser ablation inductively coupled plasma mass spectroscopy (LA-ICP-MS) at the State Key Laboratory of Geological Processes and Mineral Resources (GPMR), China University of Geosciences, Wuhan. Laser analysis was performed with a GeoLas 2005. An Agilent 7500a ICP-MS instrument was used to acquire ion-signal intensities. Helium was applied as a carrier gas. Argon was used as the make-up gas and mixed with the carrier gas via a T-connector before entering the ICP. Nitrogen was added into the central gas flow (Ar + He) of the Ar plasma to decrease the detection limit and improve precision (Hu et al., 2008). Each analysis incorporated a background acquisition of approximately 20 to 30 s (gas blank) followed by 50 s data acquisition from the sample. The Agilent Chemstation was utilized for the acquisition of each individual analysis. Off-line selection and integration of background and analyte signals, and time-drift correction and quantitative calibration for trace element analyses and U-Pb dating were performed by

ICPMSDataCal (Liu et al., 2008, 2010). Zircon 91500 was used as the external standard for U-Pb dating, and was analyzed twice every five sample analyses. Time-dependent drifts of U-Th-Pb isotopic ratios were corrected using a linear interpolation (with time) for every five analyses according to the variations of 91500 (Liu et al., 2010). Uncertainty of preferred values for the external standard 91500 was propagated to the ultimate results of the samples. Concordia diagrams and weighted mean calculations were made using Isoplot/Ex_ver3 (Ludwig, 2003).

Molybdenite Re-Os dating

Molybdenite samples representative of stage D2 quartz – molybdenite vein (DG03; Fig. 5d) and stage D3 quartz – polymetallic sulfide vein (FDG08; Fig. 5f) of the Donggou porphyry Mo deposit were collected to establish the timing of molybdenite mineralization using the Re-Os chronometer. The Carius tube method was used for dissolution of molybdenite and equilibration of the sample with tracer Re and Os (Selby and Creaser, 2001). Approximately 22-23 mg of molybdenite were dissolved and equilibrated with a known amount of ^{185}Re and isotopically normal Os at 240 °C for 24 h. Solvent extraction and microdistillation was used to separate Os, whereas anion exchange chromatography was used to separate Re (Selby and Creaser, 2001). The concentrations of ^{187}Re and ^{187}Os were determined at the Laboratory for Sulfide and Source Rock Geochronology and Geochemistry (a member of the Durham Geochemistry Centre), Durham University, using isotope dilution negative thermal ionization mass spectrometry (ID-NTIMS). Isolated and purified Re and Os solutions were loaded onto Ni and Pt filaments, respectively, and analyzed using a Thermo Scientific TRITON mass-spectrometer with Faraday collectors. Re-Os model ages were calculated by the equation, $\ln(^{187}Os/^{187}Re + 1)/\lambda$, where λ denotes the decay constant for ^{187}Re. The ^{187}Re decay constant used is 1.666×10^{-11} year^{-1}, with an uncertainty of 0.31% (Smoliar et al., 1996; Selby et al., 2007). Uncertainties in the age calculations include uncertainties associated with (1) ^{185}Re and ^{190}Os spike calibrations, (2) weighing the spikes, (3) magnification with spiking, (4) mass spectrometric measurement of isotopic ratios, (5) blanks (Re = 2.4 pg, Os = 0.1 pg, $^{187}Os/^{188}Os$ = ~0.25), and (6) the ^{187}Re decay constant.

Sericite $^{40}Ar/^{39}Ar$ dating

Sample SY02 was taken from sericitic alteration assemblages associated with a stage S2 Pb-Zn-sulfide vein of Sanyuangou. The sample is dominated by sericite that is intergrown with sphalerite and pyrite (Fig. 9f). After petrographic examination, suitable parts of the sample were crushed, repeatedly sieved to obtain mineral grains as uniform as possible in size (0.5-2 mm), washed in distilled water in

an ultrasonic bath for 1 h, and dried. Sericite aggregates of 0.5 to 1.0 mm were screened under a binocular microscope.

Sericite mineral separates were irradiated along with the ZBH-25 biotite standard (132.7 ± 1.2 Ma at 1σ; Wang, 1983) for 55 h in the Swimming Pool Reactor, Chinese Institute of Atomic Energy (Beijing). After a three month cooling period, the samples were analyzed by the $^{40}Ar/^{39}Ar$ stepwise incremental heating method using a MM-1200B mass spectrometer at Institute of Geology, Chinese Academy of Geological Sciences. The analytical procedures are detailed in Chen et al. (2002) and summarized here. The Ar extraction system comprises an electron bombardment heated furnace in which the samples were heated under vacuum. The released gases were admitted to a purification system, with 30 min for heating-extraction for each temperature increment and 30 min for purification. Purified Ar was trapped in activated charcoal finger at liquid-nitrogen temperature and then released into the mass spectrometer for isotope analysis. Measured isotopic ratios were corrected for mass discrimination, atmospheric Ar component, blanks, and irradiation-induced mass interference. The correction factors of interfering isotopes produced during irradiation were determined by analysis of irradiated K_2SO_4 and CaF_4 pure salts, and their values are $(^{36}Ar/^{37}Ar)_{Ca}$ = 0.000240, $(^{40}Ar/^{39}Ar)_K$ = 0.004782, and $(^{39}Ar/^{37}Ar)_{Ca}$ = 0.000806 (Chen et al., 2002). All dates are reported using 5.543×10^{-10} a^{-1} as the total decay constant for ^{40}K (Steiger and Jäger, 1977). The age uncertainties are reported at the 95% confidence level (2σ), and include the uncertainties in irradiation correction factors and the J value, but do not include the uncertainty in the potassium decay constant. The Ar-Ar data were calculated and plotted using Isoplot/Ex_ver3 (Ludwig, 2003).

LA-ICP-MS analyses of pyrite

Two ore samples (FDG09 and FDG11) from stage D3 Pb-Zn-sulfide vein of the Donggou porphyry Mo deposit and two samples (SY03 and SY04) from stage S2 Pb-Zn-sulfide vein of the Sanyuangou Pb-Zn-Ag deposit were selected for pyrite trace element analysis. The analysis was conducted at the Centre of Excellence in Ore Deposits (CODES), University of Tasmania, Australia. Analytical instrumentation consists of a New Wave 213-nm solid-state laser microprobe and an Agilent 7500 Quadrupole ICP-MS. The operating conditions and procedures applied to pyrite have been detailed in Large et al. (2007) and Danyushevsky et al. (2011).

Spot analyses of pyrite were performed by laser-ablating spots of 35 μm diameter. The repetition rate was 5 Hz, and laser beam energy was maintained between 4 and 5 Jcm^{-2}. Analysis time was restricted to 90 s, consisting of 30-s background (laser off) and 60-s analysis (laser on). The primary calibration standard (STDGL2b2) consists of a fused glass containing 25% Zn concentrate and 75% pyrrhotite developed in-house (Danyushevsky et al., 2011). It was analyzed twice every 1.5 hours with a 100-μm beam size at 5 Hz to correct for instrument drift. Data were reduced using SILLS software following standard methods (Longerich et al., 1996). Iron was used as the internal standard, and the Fe contents were determined by EMP analyses at the State Key Laboratory of GPMR, China University of Geosciences, Wuhan.

In-situ lead isotope analyses

Three ore samples (FDG09, FDG10, and FDG11) from stage D3 quartz – polymetallic sulfide veins at Donggou and three samples (SY04, SY05, and SY06) from stage S2 Pb-Zn-sulfide veins at Sanyuangou were selected for lead isotopic analyses to provide additional constraints on a possible genetic link between these two deposits. *In-situ* lead isotope analyses on pyrite were performed on a Neptune Plus MC-ICP-MS (Thermo Fisher Scientific, Dreieich, Germany) equipped with a Geolas 2005 excimer ArF laser ablation system (Lambda Physik, Göttingen, Germany) at the State Key Laboratory of GPMR, China University of Geosciences, Wuhan. In the laser ablation system, helium was used as the carrier gas for the ablation cell and was mixed with argon (make-up gas) after the ablation cell. The spot diameter ranged from 44 to 90 μm dependent on Pb signal intensity. The pulse frequency was from 4 to 10 Hz, but the laser fluence was kept constant at ~3 J/cm^2. A new signal-smoothing and mercury-removing device was used downstream from the sample cell to efficiently eliminate the short term variation of the signal and remove the mercury from the background and sample aerosol particles (Hu et al., 2014). The Neptune Plus was equipped with nine Faraday cups fitted with 10^{11} Ω resistors. Isotopes ^{208}Pb, ^{207}Pb, ^{206}Pb, ^{204}Pb, ^{205}Tl, ^{203}Tl and ^{202}Hg were collected in faraday cups within static mode. The mass discrimination factor for Pb was determined using a Tl solution (NIST SRM 997) nebulized at the same time as the sample, using an Aridus II desolvating nebulizer. The ^{202}Hg signal was used to correct the remained ^{204}Hg interference on ^{204}Pb, using the natural $^{202}Hg/^{204}Hg$ ratio.

In this method, the natural Tl-isotopic composition was assumed. MASS-1, a sulfide standard reference from USGS (Wilson et al., 2002), and two in-house standards PY-3 and Sph-2 were then run to define the mathematical relationship between Tl and Pb mass bias (Woodhead, 2002). The Pb isotopic compositions of those three sulfides samples were previously determined by solution MC-ICPMS at GPMR. MASS-1 was used to monitor the precision and accuracy of the measurements after ten sample analysis, over the entire period of analysis. The obtained accuracy is estimated to be equal to or better than ± 0.6 ‰ for $^{208}Pb/^{204}Pb$, $^{207}Pb/^{204}Pb$, and $^{206}Pb/^{204}Pb$ compared to the solution value by MC-ICP-MS, with a typical precision of 0.4 ‰ (2σ).

Results

Geochronological data

Zircon U-Pb ages

The U-Pb isotope data are tabulated in Appendix 1 and illustrated in concordia diagrams (Fig. 11). Zircon grains from the Donggou granite porphyry are euhedral to subhedral, 30-200 μm long, with aspect ratios of 1 to 2.5. Most zircon grains show oscillatory zoning in CL images (Fig. 11a), consistent with a magmatic origin. These zircons have high Th (177-1911 ppm) and U (279-3722 ppm), with Th/U ratios ranging from 0.43 to 1.71, which is typical of magmatic zircons (Claesson et al., 2000). A total of thirteen spot analyses were made on twelve zircon grains for sample DG01. Eleven spots are concordant, with the remaining two being slightly discordant (Fig. 11a). However, the discordant data have $^{206}Pb/^{238}Pb$ ages indistinguishable from the concordant ones (Appendix 1), indicating that the discordance may reflect uncertainties related to ^{207}Pb measurement or common Pb correction, rather than lead loss. All thirteen analyses have a weighted mean $^{206}Pb/^{238}U$ age of 117.8 ± 0.9 Ma (1σ, MSWD = 0.1; Fig. 11a).

Zircon grains from the Sanyuangou quartz diorite are euhedral to subhedral, 50-200 μm long, with aspect ratios of 1 to 2. In CL images, most zircon grains show oscillatory zoning (Fig. 11b). These grains have relatively high Th (358-2,403 ppm) and U (393-1,350 ppm), with Th/U ratios of 0.69 to 1.79 (Appendix 1). Fourteen spot analyses were made on 14 zircon grains for sample SY01. The spots are concordant and yield a weighted mean $^{207}Pb/^{206}Pb$ age of 1,756 ± 9 Ma (1σ, MSWD = 1.1; Fig. 11b).

Zircon grains from the Wangpingxigou quartz monzonite are euhedral and display well-developed prismatic and pyramidal faces. They are commonly 100-300 μm long with length/width ratios of 1 to 3. Most zircon grains show spectacular oscillatory zoning in CL images (Fig. 11c). These grains contain 167-993 ppm Th and 214-885 ppm U, with Th/U ratios of 0.65 to 1.48 (Appendix 1). Fifteen spot analyses on 14 zircon grains from sample WP01 yield concordant ages with a weighted mean $^{207}Pb/^{206}Pb$ age of 1,837 ± 11 Ma (1σ, MSWD = 1.1; Fig. 11c).

Molybdenite Re-Os ages

Re-Os isotope data are presented in Table 1. All age uncertainties are quoted at the 2σ level. Sample from the quartz – molybdenite vein (DG03) contains 2.6 ppm Re and 3.2 ppb ^{187}Os, and has a Re-Os model age of 117.5 ± 0.8 [0.9] Ma (bracketed value refers to errors including the decay constant uncertainty). Sample from the quartz – polymetallic sulfide vein (FDG08) contains 7.1 ppm Re and 8.6 ppb ^{187}Os, and has a Re-Os model age of 116.4 ± 0.6 [0.7] Ma. The age difference between sample DG03 and FDG08 is consistent with field relationship and paragenetic sequence between the stage D2 quartz – molybdenite vein and stage D3 quartz – polymetallic sulfide vein.

Sericite $^{40}Ar/^{39}Ar$ age

The $^{40}Ar/^{39}Ar$ results of sample SY02 are summarized in Table 2 and the age spectrum and inverse isochron are shown in Figure 12. All $^{40}Ar/^{39}Ar$ ages are calculated using the decay constants of Steiger and Jäger (1977) and the uncertainties are reported at the 95 % confidence level (2σ). The sample yields a well-defined plateau age of 115.9 ± 0.9 Ma (MSWD = 0.7), consisting of seven contiguous steps that account for 92.7 % of the total ^{39}Ar released (Fig. 12a). Isotopic results of these steps formed a well-defined inverse isochron in the $^{39}Ar/^{40}Ar$ versus $^{36}Ar/^{40}Ar$ diagram (Fig. 12b), with an inverse isochron age of 116.0 ± 1.2 Ma (MSWD = 10.9) that is indistinguishable from the plateau age. The inverse isochron plot has a $^{40}Ar/^{36}Ar$ ratio of 299.0 ± 6.0, which is within uncertainty of the accepted value of the present air (298.5 ± 0.3; Renne et al., 2009) and thus suggests that no excessive argon was incorporated into the mineral.

Trace element compositions of pyrite

A total of 50 LA-ICP-MS spot analyses were made on pyrite grains from the Donggou porphyry Mo and Sanyuangou Pb-Zn-Ag vein deposits. The trace element analyzed include Cr, Mn, Fe, Co, Ni,

Cu, Zn, Ga, As, Se, Mo, Ag, Cd, Sn, Sb, Te, Ba, Gd, Hf, Ta, W, Pt, Au, Tl, Pb and Bi. The full analytical results are listed in Appendix 2, and the compositions of selected trace elements are illustrated in Figure 13. Pyrite from the Donggou porphyry Mo deposit is depleted in most trace elements, but contains higher Mo (up to 154 ppm) and Bi (29 ppm) compared to pyrite from the Sanyuangou Pb-Zn-Ag vein deposit. Pyrite from Donggou also contains considerable Sn (0.10 to 6 ppm), Te (0.07 to 9.7 ppm), Pb (0.07 to 398 ppm), As (1.76 to 1821 ppm), and Sb (0.01 to 31 ppm). In contrast, pyrite from Sanyuangou has elevated Cu (2.7 to 23,420 ppm), Zn (0.25 to 26,893 ppm), Pb (0.02 to 637 ppm), Ag (up to 1091 ppm), Au (up to 21 ppm), and As (0.3 to 17913 ppm). Pyrites from Donggou and Sanyuangou have similar Co (0.1-1224 vs. 0.5-1290 ppm) and Ni (0.1-116 vs. 0.3-300 ppm) contents and Co/Ni ratios (0.7-48 vs. 0.4-82; Fig. 14).

Pyrite lead isotopic compositions

The *in-situ* lead isotope analyses of pyrite are listed in Table 3. Ten pyrite grains from Donggou have $^{206}Pb/^{204}Pb$ ratios of 17.328 to 17.517, $^{207}Pb/^{204}Pb$ of 15.408 to 15.551, and $^{208}Pb/^{204}Pb$ of 38.080 to 38.436. Pyrite grains from Sanyuangou have Pb isotopic compositions that are very similar to that of Donggou ($^{206}Pb/^{204}Pb$ = 17.273 to 17.495; $^{207}Pb/^{204}Pb$ = 15.431 to 15.566; $^{208}Pb/^{204}Pb$ = 37.991 to 38.337; n = 10).

Discussion

Timing of mineralization

Donggou porphyry Mo deposit

Zircon grains from the Donggou granite porphyry show morphological and compositional features typical of magmatic zircons (Claesson et al., 2000; Wu and Zheng, 2004; Appendix 1). The precise LA-ICP-MS zircon U-Pb age (117.8 ± 0.9 Ma) presented here provides a tight constraint on the emplacement age of the Donggou porphyry. This age is consistent, within analytical uncertainty, with a previous LA-ICP-MS zircon U-Pb age (117 ± 1 Ma) for the Donggou porphyry (Dai et al., 2009). The younger zircon U-Pb ages (112 ± 1 Ma by SHRIMP, Ye et al., 2006; 114 ± 1 Ma by LA-ICP-MS, Dai et al., 2009) either reflect multistage magmatism at Donggou or different analytical protocols used by those authors. However, our field observations and drill core logging did not identify evidence for

multiple intrusions, nor did the authors who obtained the younger U-Pb ages presented evidence that their samples were from intrusions other than Donggou porphyry. Thus it is suggested that the different ages have more likely resulted from different analytical methods or from the analysis of zircon grains that have experienced Pb loss.

The molybdenite Re-Os chronometer is remarkably robust due to the high closure temperature of Re-Os isotopes in molybdenite (Suzuki et al., 1996; Stein et al., 2001; Selby et al., 2002; Chiaradia et al., 2013). Thus, Re-Os dating of this mineral commonly provides reliable constraints on the timing of ore formation (Selby et al., 2002). Molybdenite from the stages D2 and D3 veins of the Donggou Mo deposit have overlapping Re-Os model ages of 117.5 ± 0.8 Ma and 116.4 ± 0.6 Ma (Table 1). The molybdenite Re-Os ages are in excellent agreement with zircon U-Pb age of the Mo mineralized porphyry, providing strong evidence for temporal and genetic relationship between magmatism and Mo mineralization. The absolute value of molybdenite Re-Os age of the stage D3 quartz – polymetallic sulfide vein (116.4 ± 0.6 Ma) is slightly younger than that of the stage D2 quartz – molybdenite vein (117.5 ± 0.8 Ma) and zircon U-Pb age (117.0 ± 1 Ma) of the Donggou porphyry, but they are all indistinguishable if the analytical uncertainties are considered. Based on these results, we propose that the Donggou porphyry Mo deposit formed between 117.5 ± 0.8 Ma and 116.4 ± 0.6 Ma during the Early Cretaceous, genetically associated with the Donggou porphyry.

Sanyuangou Pb-Zn-Ag vein deposit

Field and petrographic relations (Fig. 9f) indicate that sericite is spatially and texturally associated with stage S2 Pb-Zn sulfide veins at Sanyuangou, and thus $^{40}Ar/^{39}Ar$ dating of sericite can provide constraints on the timing of hydrothermal alteration and mineralization (Li et al., 2003; Chiaradia et al., 2013). One sericite sample has a $^{40}Ar/^{39}Ar$ plateau age of 115.9 ± 0.9 Ma and an identical inverse isochron age of 116.0 ± 1.2 Ma (Fig. 12), which represent the time when sericite cooled below the closure temperature of argon isotopes in mica. Formation of Pb-Zn-Ag veins at Sanyuangou has been constrained at 206°-265°C based on the sulfur isotopic equilibration equations of pyrite-galena and sphalerite-galena pairs from stage S2 veins (Li, 2013). This temperature range is lower than the argon closure temperature in mica (300°-350°C; McDougall and Harrison, 1999), the present $^{40}Ar/^{39}Ar$ age can therefore be reliably interpreted as the timing of hydrothermal alteration and Pb-Zn-Ag mineralization of the Sanyuangou deposit. Ye et al. (2006) reported a sericite $^{40}Ar/^{39}Ar$ "plateau" age of 110.1 ± 9.2 Ma (24.2 % of the total ^{39}Ar released) for Sanyuangou, which overlaps with our new

475 $^{40}Ar/^{39}Ar$ data but has a significantly larger uncertainty. Our new $^{40}Ar/^{39}Ar$ age therefore provides an
476 improved and tight constraint for the timing of mineralization at Sanyuangou.

477 Zircon grains from the Sanyuangou quartz diorite stock hosting the Pb-Zn-Ag mineralization have
478 a weighted mean $^{207}Pb/^{206}Pb$ age of 1,756 ± 9 Ma (Fig. 11b), which is considered to be the
479 emplacement age of this intrusion. To the east of the Sanyuangou quartz diorite, the Wangpingxigou
480 quartz monzonite has a $^{207}Pb/^{206}Pb$ age of 1,837 ± 11 Ma (Fig. 11c), which predates the Sanyuangou
481 quartz diorite stock by 80-100 m.y. Thus, these two intrusions are products of two episodes of granitoid
482 magmatism during the Late Paleoproterozoic. The present LA-ICP-MS zircon U-Pb and sericite
483 $^{40}Ar/^{39}Ar$ dating results demonstrate that the Sanyuangou Pb-Zn-Ag deposits formed during the Early
484 Cretaceous and significantly postdate the host quartz diorite and quartz monzonite. Consequently, a
485 possible genetic link between the host intrusion and mineralization, as previously suggested (HBGMR,
486 1989), can be ruled out.

487 **A porphyry-related Mo-Pb-Zn-Ag metallogenic system**

488 The Sanyuangou Pb-Zn-Ag vein deposit is located about 3 km south of the Donggou porphyry
489 Mo deposit (Fig. 2). Sericite $^{40}Ar/^{39}Ar$ dating of the alteration assemblages proximal to a Stage S2 Pb-
490 Zn-sulfide vein (115.9 ± 0.9 Ma) at Sanyuangou and Re-Os dating of molybdenite from Stage D2
491 quartz – molybdenite vein (117.5 ± 0.8 Ma) and Stage D3 quartz – polymetallic sulfide vein (116.4 ±
492 0.6 Ma) at Donggou suggest that Pb-Zn-Ag mineralization at Sanyuangou was mutually consistent.
493 Therefore, the close spatial-temporal relations between the Sanyuangou Pb-Zn-Ag and Donggou
494 porphyry Mo deposits propose a genetic association.

495 Pyrite is an important scavenger of a variety of trace elements as Au, Ag, Cu, Pb, Zn, Co, Ni, As,
496 Sb, Se, Te, Hg, Tl, and Bi (Cook and Chryssoulis, 1990; Craig et al., 1998; Large et al., 2007; Reich et
497 al., 2013) and thereby can provide useful information on the composition and evolution of ore fluids
498 (Hawley and Nichol, 1961; Bralia et al., 1979; Craig et al., 1998; Morey et al., 2008; Large et al., 2007,
499 2009, 2011). Knowledge on the trace-element geochemistry of pyrite not only contributes to a better
500 understanding in the physicochemical parameters of ore fluids from which pyrite precipitated and thus
501 a more geologically reasonable metallogenic model for the pyrite-dominated deposits, but also
502 improves exploration strategies of these deposits (Heinrich et al., 2003; Danyushevsky et al., 2011).

503 Laser ablation ICP-MS spot analyses show that pyrite from Donggou is enriched in Mo and Bi (Fig.
504 13). In contrast, pyrite from Sanyuangou is depleted in Mo and Bi, but enriched in Cu, Zn, Pb, Ag, Au,
505 and As (Fig. 13). The trace element patterns of pyrite from these two deposits are consistent with metal
506 zonation typically observed in a porphyry-related hydrothermal system, commonly illustrated by Cu,
507 Mo → Zn, Pb → Ag, Au, As from porphyry ores to distal base-metal veins (Emmons, 1927; Jones,
508 1992; Seedorff et al., 2005; Sillitoe, 2010). On the other hand, pyrite from Sanyuangou has contents of
509 Sn, Sb, Co, and Ni similar to those from Donggou, with comparable Co/Ni ratios mostly higher than 1
510 (Figs. 13, 14). This observation also is supportive for a magmatic-hydrothermal origin for the
511 Sanyuangou Pb-Zn-Ag deposit (Bralia et al., 1979; Deol et al., 2012).

512 Pyrite may contain moderate to high quantities of Pb, but virtually lacks U, and therefore its Pb
513 isotopic compositions provide valuable information on the sources of lead and associated metals
514 (Meffre et al., 2008; Woodhead et al., 2009; Darling et al., 2012; Steadman et al., 2013). *In-situ* pyrite
515 isotopic compositions of Donggou and Sanyuangou are used to uncover a possible genetic link between
516 these two deposits. Pyrite from Sanyuangou has Pb isotopic compositions ($^{206}Pb/^{204}Pb$ = 17.273-17.495,
517 $^{207}Pb/^{204}Pb$ = 15.431-15.566, and $^{208}Pb/^{204}Pb$ = 37.991-38.337) that are similar to values of pyrite from
518 Donggou ($^{206}Pb/^{204}Pb$ = 17.328-17.517, $^{207}Pb/^{204}Pb$ = 15.408-15.551, and $^{208}Pb/^{204}Pb$ = 38.080-38.436).
519 Thorogenic (Fig. 15a) and uranogenic (Fig. 15b) Pb isotopic diagrams show that the pyrite samples
520 from the two deposits plot in the same area and display similar trends, indicating a common source of
521 the lead. Collectively, field, paragenetic, geochronological, geochemical, and isotopic data indicate that
522 the Pb-Zn-Ag mineralization at Sanyuangou is genetically related to the Donggou porphyry Mo system,
523 and can be best interpreted as a distal product of the Donggou magmatic-hydrothermal system.

524 There are additional Pb-Zn-Ag vein deposits surrounding the Donggou porphyry Mo deposit
525 (e.g., Wangpingxigou, Laodaizhanggou; Fig. 2). These deposits have geological and mineralization
526 characteristics consistent with the Sanyuangou deposit (Huang et al., 1992; Ye, 2006; Yao et al., 2008).
527 The Wangpingxigou deposit has a sphalerite Rb-Sr isochron age of 117 ± 27 Ma (Yao et al., 2010).
528 This age, although having a large analytical uncertainty, indicates that Wangpingxigou formed in Early
529 Cretaceous, broadly synchronous with the Pb-Zn-Ag veins at Sanyuangou. However, ore-related
530 sericite from the Laodaizhanggou Pb-Zn-Ag vein deposit yields a well-defined $^{40}Ar/^{39}Ar$ plateau age of
531 124.7 ± 1.2 Ma (Li, 2013), which is about 7 m. y. older than Sanyuangou (115.9 ± 0.9 Ma; Fig. 12a)
532 and Donggou (117.5 ± 0.8 Ma to 116.4 ± 0.6 Ma; Table 1). As such, the age indicate that district-wide

Pb-Zn-Ag mineralization may have formed in association with multiple magmatic-hydrothermal activities.

Early Cretaceous magmatic activity is well-recognized at Waifangshan and surrounding districts. The Taishanmiao pluton, with an exposure of ca. 290 km^2 in southwest of the Fudian ore field (Figs. 1, 2), formed by episodic magmatism from 125 to 115 Ma as revealed by zircon U-Pb dating (Ye et al., 2008; Qi, 2014; Gao et al., 2014). In the east of Taishanmiao, the Zhuyuangou quartz-molybdenite veins (0.1 Mt Mo; Huang et al., 2010) are hosted in fine-grained granite and have molybdenite Re-Os ages of 122.2 ± 2.3 and 119.6 ± 2.2 Ma (Huang et al., 2010). Taken together, we suggest that the Pb-Zn-Ag vein deposits in the Fudian ore field could have been products of multiple magmatic-hydrothermal events in the Early Cretaceous, with some (e.g., Sanyuangou and Wangpingxigou) being related to the Donggou mineralized porphyry, but others (e.g., Laodaizhanggou) likely having an association with earlier magmatism as represented by the Taishanmiao intrusive complex and Zhuyuangou quartz-molybdenite veins (Huang et al., 2010).

Implications for mineral exploration

Our study has shown that the Pb-Zn-Ag veins in the Fudian ore field are most likely distal products of porphyry-related magmatic-hydrothermal systems. This view has significant implications for Mo and Pb-Zn-Ag mineral exploration in the area, as these two mineralization styles can be used as a vector for each other (Sillitoe, 2010). The Pb-Zn-Ag veins commonly occur in shallow and distal parts of a porphyry system. The fault zones surrounding known porphyry Mo deposits are favorable sites for localizing Pb-Zn-Ag veins (Seedorff et al., 2005; Sillitoe, 2010). Brittle faults with different strikes are well developed in the Fudian ore field (Fig. 2), some of which are marked by variable degrees of hydrothermal alteration. Such structures are good targets for Pb-Zn-Ag veins. Other districts along the southern NCC also host giant porphyry and porphyry-skarn Mo deposits that formed during the Late Jurassic to Early Cretaceous (Fig. 1), including Jinduicheng (Huang et al., 1994), Nannihu (Li et al., 2003), Leimengou (Li et al., 2006), and Yuchiling (Li et al., 2012d, 2013a). Our model in the Fudian ore field has broad implications for exploration of Pb-Zn-Ag deposits in those districts, where fractures zones, particularly those with extensive hydrothermal alteration, should be good targets for Pb-Zn-Ag resources.

561 The Pb-Zn-Ag veins are widespread in large areas of the southern NCC (Fig. 1). Although some
562 veins show close spatial and temporal relationships with porphyry Mo deposits (Fig. 1), such a
563 relationship, however, is lacking for other vein deposits. This contrast may reflect the variable degree
564 of erosion of each district and/or the difference in emplacement depth of individual Mo mineralized
565 porphyry systems. We predict that unexposed porphyry Mo deposits may occur beneath and/or to the
566 side of some Pb-Zn-Ag veins where magmatic intrusions are lacking at surface. The Pb-Zn-Ag veins at
567 Laodaizhanggou (Fig. 2) may be such an example. These veins predate the Donggou porphyry Mo
568 deposit by ca. 7 m.y. and thus are unlikely formed by magmatic-hydrothermal fluids from Donggou.
569 Laodaizhanggou is broadly coeval with the Taishanmiao intrusive complex and the Zhuyuangou quartz
570 – molybdenite veins, but the large distance between the former and the latter (>8 km; Fig. 2) suggests
571 that genetic link with the Taishanmiao magmatism is less likely. We therefore suggest that a concealed
572 magmatic intrusion, possibly with Mo mineralization, is located at depth beneath and/or to the side of
573 Laodaizhanggou. Given the distribution of Pb-Zn-Ag vein deposits in the area, we propose that a
574 porphyry Mo deposit may be located at depth between Laodaizhanggou, Xizaogou, and Liezishan (Fig.
575 2).

576 Silver-Pb-Zn veins are particularly developed in the Xiayu ore field, to the west of the
577 Xiong'ershan district (Fig. 1). These veins have been the largest silver and an important Pb + Zn
578 producer in central China (Chen et al., 2004; Mao et al., 2006; Li et al., 2013b). Previous studies favor
579 a magmatic origin for these Ag-Pb-Zn veins (Fig. 1; Mao et al., 2006; Ye, 2006; Gao et al., 2010a,
580 2011). While no porphyry Mo deposits have been recognized, as yet, with these large Ag-Pb-Zn
581 resources in the Xiayu ore field, we propose that Xiayu ore field may be a potential exploration target
582 for porphyry Mo deposits.

583 ## Conclusions

584 The Fudian ore field in the southern NCC contains the Donggou porphyry Mo deposit and several
585 Pb-Zn-Ag vein deposits (e.g., Sanyuangou, Wangpingxigou, Laodaizhanggou). New geochronological
586 data show that the Donggou porphyry (LA-ICP-MS zircon U-Pb = 117.8 ± 0.9 Ma), the Donggou Mo
587 deposit (molybdenite Re-Os = 117.5 ± 0.8 and 116.4 ± 0.6 Ma), and the Sanyuangou Pb-Zn-Ag veins
588 (sericite $^{40}Ar/^{39}Ar$ = 115.9 ± 0.9) formed contemporaneously in a short period during the Early

589 Cretaceous. Trace element compositions of pyrite from Donggou and Sanyuangou are consistent with
590 metal zonation from central Mo ores to peripheral Pb-Zn-sulfide veins, typical of porphyry Cu/Mo
591 deposits worldwide. *In-situ* lead isotopic analysis of pyrite suggests a common metal source for the
592 Donggou porphyry Mo deposit and Sanyuangou Pb-Zn-Ag vein deposit. The trace element and lead
593 isotope data of pyrite thus confirm a magmatic-hydrothermal origin for the Sanyuangou Pb-Zn-Ag
594 veins and its genetic link to the Donggou porphyry Mo deposit. Recognition of a porphyry-related
595 magmatic-hydrothermal system in the Fudian ore field has significant implications for future
596 exploration of Mo and Pb-Zn-Ag resources in the southern NCC. Where either base metal veins or
597 porphyry Mo ore bodies are known in a given area, they provide a potential exploration vector for the
598 other mineralization style.

599 ## Acknowledgments

600 We acknowledge financial supports of National Natural Science Foundation of China (41325007,
601 41402066, 91414301, 91514303) and the Australian Research Council through the Industrial
602 Transformation Research Hub grant and Centre of Excellence Funding Programs. Mr. Ji-Xiang Sui and
603 Xiao-Ye Jin provided help during the fieldwork. We are indebted to Prof. Leonid Danyushevsky and
604 Sarah Gilbert for assistance with LA-ICPMS analyses at CODES, University of Tasmania. Prof. Xin-
605 Fu Zhao are thanked for his insights on an early draft of this paper. The paper benefitted a lot from
606 careful reviews by two anonymous reviewers. Our thanks extend to Profs. Franco Pirajno (Editor-in-
607 Chief) and Yan-Jing Chen (Associate Editor) for editorial handling.
608

609 ## References

610 Babcock, R.C., Ballantyne, G.H., Phillips, C.H., 1995. Summary of the geology of the Bingham district,
611 Utah. Porphyry copper deposits of the American Cordillera: Arizona Geological Society Digest 20,
612 316-335.
613 Bralia, A., Sabatini, G., Troja, F., 1979. A reevaluation of the Co/Ni ratio in pyrite as geochemical tool
614 in ore genesis problems. Miner. Deposita 14, 353-374.
615 Catchpole, H., Kouzmanov, K., Putlitz, B., Seo, J.H., Fontboté, L., 2015. Zoned base metal

616 mineralization in a porphyry system: Origin and evolution of mineralizing fluids in the Morococha
617 district, Peru. Econ. Geol. 110, 39-71.
618 Chen, W., Zhang, Y., Ji, Q., Wang, S., Zhang, J., 2002. Magmatism and deformation times of the
619 Xidatan rock series, East Kunlun Mountains. Science in China Series B: Chemistry 45, 20-27.
620 Chen, Y.J., Fu, S.G., 1992. Gold mineralization in West Henan, China. China Seismological Press,
621 Beijing, 234 pp (in Chinese with English abstract).
622 Chen, Y.J., Li, C., Zhang, J., Li, Z., Wang, H.H., 2000. Sr and O isotopic characteristics of porphyries
623 in the Qinling molybdenum deposit belt and their implication to genetic mechanism and type.
624 Science in China Series D: Earth Sciences 43, 82-94.
625 Chen, Y.J., Pirajno, F., Sui, Y.H., 2004. Isotope geochemistry of the Tieluping silver-lead deposit,
626 Henan, China: A case study of orogenic silver-dominated deposits and related tectonic setting.
627 Miner. Deposita 39, 560-575.
628 Chen, Y.J., Wang, P., Li, N., Yang, Y.F., Pirajno, F., 2016. The collision-type porphyry Mo deposits in
629 Dabie Shan, China. Ore Geol. Rev. doi:10.1016/j.oregeorev.2016.03.025.
630 Chiaradia, M., Schaltegger, U., Spikings, R., Wotzlaw, J., Ovtcharova, M., 2013. How accurately can
631 we date the duration of magmatic-hydrothermal events in porphyry systems?-an invited paper,
632 Econ. Geol. 108, 565-584.
633 Claesson, S., Vetrin, V., Bayanova, T., Downes, H., 2000. U-Pb zircon ages from a Devonian
634 carbonatite dyke, Kola peninsula, Russia: a record of geological evolution from the Archaean to the
635 Palaeozoic. Lithos 51, 95-108.
636 Cook, N.J., Chryssoulis, S.L., 1990. Concentrations of invisible gold in the common sulfides. The
637 Canadian Mineralogist 28, 1-16.
638 Cooke, D.R., Hollings, P., Walshe, J.L., 2005. Giant porphyry deposits: characteristics, distribution,
639 and tectonic controls. Econ. Geol. 100, 801-818.
640 Coplen, T.B., Kendall, C., Hopple, J., 1983. Comparison of stable isotope reference samples. Nature
641 302, 236-238.
642 Craig, J.R., Vokes, F.M., Solberg, T.N., 1998. Pyrite: physical and chemical textures. Miner. Deposita
643 34, 82-101.
644 Dai, B.Z., Jiang, S.Y., Wang, X.L., 2009. Petrogenesis of the granitic porphyry related to the giant
645 molybdenum deposit in Donggou, Henan province, China: Constraints from petrogeochemistry,

zircon U-Pb chronology and Sr-Nd-Hf isotopes. Acta Petrol. Sin. 25, 2889-2901(in Chinese with English abstract).

Danyushevsky, L., Robinson, P., Gilbert, S., Norman, M., Large, R., McGoldrick, P., Shelley, M., 2011. Routine quantitative multi-element analysis of sulphide minerals by laser ablation ICP-MS: Standard development and consideration of matrix effects. Geochemistry: Exploration, Environment, Analysis 11, 51-60.

Darling, J.R., Storey, C.D., Hawkesworth, C.J., Lightfoot, P.C., 2012. In-situ Pb isotope analysis of Fe-Ni-Cu sulphides by laser ablation multi-collector ICPMS: New insights into ore formation in the Sudbury impact melt sheet. Geochim. Cosmochim. Ac. 99, 1-17.

Deol, S., Deb, M., Large, R.R., Gilbert, S., 2012. LA-ICPMS and EPMA studies of pyrite, arsenopyrite and loellingite from the Bhukia-Jagpura gold prospect, southern Rajasthan, India: Implications for ore genesis and gold remobilization. Chem. Geol. 326, 72-87.

Dilles, J.H., Einaudi, M.T., 1992. Wall-rock alteration and hydrothermal flow paths about the Ann-Mason porphyry copper deposit, Nevada; a 6-km vertical reconstruction. Econ. Geol. 87, 1963-2001.

Dong, Y.P., Zhang, G.W., Neubauer, F., Liu, X.M., Genser, J., Hauzenberger, C., 2011. Tectonic evolution of the Qinling orogen, China: review and synthesis. J. Asian Earth Sci. 41, 213-237.

Emmons, S.F., 1927. Geology and ore deposits of the Leadville mining district, Colorado. US Government Printing Office.

Fan, H., Xie, Y., Zhao, R., Wang, Y., 2000. Dual origins of Xiaoqinling gold-bearing quartz veins: Fluid inclusion evidence. Chinese Sci. Bull. 45, 1424-1430.

Gao, J.J., Mao, J.W., Chen, M.H., Ye, H.S., Zhang, J.J., Li, Y.F., 2011. Vein structure analysis and $^{40}Ar/^{39}Ar$ dating of sericite from sub-ore altered rocks in the Tieluping large-size Ag-Pb deposit of western Henan province. Acta Geol. Sin. 85, 1172-1187 (in Chinese with English abstract).

Gao, J.J., Mao, J.W., Ye, H.S., Chen, M.H., Zheng, R.F., 2010a. Geology and ore-forming fluid of silver-lead-zinc lode deposit of Shagou, western Henan Province. Acta Petrol. Sin. 26, 740-756 (in Chinese with English abstract).

Gao, X.Y., Zhao, T., Bao, Z.W., Yang, A.Y., 2014. Petrogenesis of the early Cretaceous intermediate and felsic intrusions at the southern margin of the North China Craton: Implications for crust-mantle interaction. Lithos 206, 65-78.

Gao, X.Y., Zhao, T.P., Yuan, Z.L., Zhou, Y.Y., Gao, J.F., 2010b. Geochemistry and petrogenesis of the Heyu batholith in the southern margin of the North China block. Acta Petrol. Sin. 26, 3485-3506 (in Chinese with English abstract).

Hart, S.R., 1984. A large-scale isotope anomaly in the Southern Hemisphere mantle. Nature 309, 753-757.

Hawley, J.E., Nichol, I., 1961. Trace elements in pyrite, pyrrhotite and chalcopyrite of different ores. Econ. Geol. 56, 467-487.

HBGMR, 1989. Regional geology of Henan Province. Geological Publishing House, Beijing, 772 pp (in Chinese).

He, Y.H., Zhao, G.C., Sun, M., Xia, X.P., 2009. SHRIMP and LA-ICP-MS zircon geochronology of the Xiong'er volcanic rocks: Implications for the Paleo-Mesoproterozoic evolution of the southern margin of the North China Craton. Precambrian Res. 168, 213-222.

Heinrich, C.A., Pettke, T., Halter, W.E., Aigner-Torres, M., Audétat, A., Günther, D., Hattendorf, B., Bleiner, D., Guillong, M., Horn, I., 2003. Quantitative multi-element analysis of minerals, fluid and melt inclusions by laser-ablation inductively-coupled-plasma mass-spectrometry. Geochim. Cosmochim. Ac. 67, 3473-3497.

Hu, S.X., Lin, Q.L., Chen, Z.M., Li, S.M., 1988. Geology and metallogeny of the collision belt between the North and the South China plates. Nanjing University Press, 558 pp (in Chinese with English abstract).

Hu, Z.C., Gao, S., Liu, Y.S., Hu, S.H., Chen, H.H., Yuan, H.L., 2008. Signal enhancement in laser ablation ICP-MS by addition of nitrogen in the central channel gas. J. Anal. Atom. Spectrom. 23, 1093-1101.

Hu, Z.C., Zhang, W., Liu, Y.S., Gao, S., Li, M., Zong, K.Q., Chen, H.H., Hu, S.H., 2014. "Wave" signal-smoothing and mercury-removing device for laser ablation quadrupole and multiple collector ICPMS analysis: application to lead isotope analysis. Anal. Chem. 87, 1152-1157.

Huang, D.H., Wu, C.Y., Du, A.D., He, H.L., 1994. Re-Os isotopic dating of molybdenite and its implication for molybdenum deposits in east Qinling area. Mineral Deposits 13, 221-230 (in Chinese with English abstract).

Huang, F., Luo, Z.H., Lu, X.X., Chen, B.H., Yang, Z.F., 2010. Geological characteristics, metallogenic epoch and geological significance of the Zhuyuangou molybdenum deposit in Ruyang area, Henan,

China. Geological Bulletin of China 29, 1704-1711 (in Chinese with English abstract).

Huang, R.Y., Qiao, H.D., Zhang, W., 1992. Ore-controlling geological conditions and metallogenic mechanism study of Pb-Zn deposits at Southern Ruyang. Henan Geology 10, 81-88 (in Chinese with English abstract).

Jones, B.K., 1992. Application of metal zoning to gold exploration in porphyry copper systems. J. Geochem. Explor. 43, 127-155.

Lang, J.R., Eastoe, C.J., 1988. Relationships between a porphyry Cu-Mo deposit, base and precious metal veins and Laramide intrusions, Mineral Park, Arizona. Econ. Geol. 83, 551-567.

Large, R.R., Bull, S.W., Maslennikov, V.V., 2011. A carbonaceous sedimentary source-rock model for Carlin-type and orogenic gold deposits. Econ. Geol. 106, 331-358.

Large, R.R., Danyushevsky, L., Hollit, C., Maslennikov, V., Meffre, S., Gilbert, S., Bull, S., Scott, R., Emsbo, P., Thomas, H., 2009. Gold and trace element zonation in pyrite using a laser imaging technique: implications for the timing of gold in orogenic and Carlin-style sediment-hosted deposits. Econ. Geol. 104, 635-668.

Large, R.R., Maslennikov, V.V., Robert, F., Danyushevsky, L.V., Chang, Z., 2007. Multistage sedimentary and metamorphic origin of pyrite and gold in the giant Sukhoi Log deposit, Lena gold province, Russia. Econ. Geol. 102, 1233-1267.

Lawley, C., Richards, J.P., Anderson, R.G., Creaser, R.A., Heaman, L.M., 2010. Geochronology and geochemistry of the MAX porphyry Mo deposit and its relationship to Pb-Zn-Ag mineralization, Kootenay arc, southeastern British Columbia, Canada. Econ. Geol. 105, 1113-1142.

Li, J.W., Bi, S.J., Selby, D., Chen, L., Vasconcelos, P., Thiede, D., Zhou, M.F., Zhao, X.F., Li, Z.K., Qiu, H.N., 2012a. Giant Mesozoic gold provinces related to the destruction of the North China craton. Earth Planet. Sc. Lett. 349, 26-37.

Li, J.W., Li, Z.K., Zhou, M.F., Chen, L., Bi, S.J., Deng, X.D., Qiu, H.N., Cohen, B., Selby, D., Zhao, X.F., 2012b. The Early Cretaceous Yangzhaiyu lode gold deposit, North China Craton: A link between craton reactivation and gold veining. Econ. Geol. 107, 43-79.

Li, J.W., Vasconcelos, P.M., Zhang, J., Zhou, M.F., Zhang, X.J., Yang, F.H., 2003. $^{40}Ar/^{39}Ar$ constraints on a temporal link between gold mineralization, magmatism, and continental margin transtension in the Jiaodong gold province, eastern China. The Journal of geology 111, 741-751.

Li, N., Chen, Y., Pirajno, F., Gong, H., Mao, S., Ni, Z., 2012c. LA-ICP-MS zircon U-Pb dating, trace

element and Hf isotope geochemistry of the Heyu granite batholith, eastern Qinling, central China: implications for Mesozoic tectono-magmatic evolution. Lithos 142, 34-47.

Li, N., Chen, Y., Pirajno, F., Ni, Z., 2013a. Timing of the Yuchiling giant porphyry Mo system, and implications for ore genesis. Miner. Deposita 48, 505-524.

Li, N., Chen, Y.J., McNaughton, N.J., Ling, X.X., Deng, X.H., Yao, J.M., Wu, Y.S., 2015. Formation and tectonic evolution of the khondalite series at the southern margin of the North China Craton: Geochronological constraints from a 1.85-Ga Mo deposit in the Xiong'ershan area. Precambrian Res. 269, 1-17.

Li, N., Chen, Y.J., Zhang, H., Zhao, T.P., Deng, X.H., Wang, Y., Ni, Z.Y., 2007. Molybdenum deposits in east Qinling. Earth Science Frontiers 14, 186-198 (in Chinese with English abstract).

Li, N., Ulrich, T., Chen, Y., Thomsen, T.B., Pease, V., Pirajno, F., 2012d. Fluid evolution of the Yuchiling porphyry Mo deposit, East Qinling, China. Ore Geol. Rev. 48, 442-459.

Li, S.G., Xiao, Y.L., Liu, D.L., Chen, Y.Z., Sun, S.S., Hart, S.R., Wang, S.S., 1993. Collision of North China and Yangtze blocks and formation of coesite-bearing eclogites: Timing and processes. Chem. Geol. 109, 89-111.

Li, Y.F., Mao, J.W., Bai, F.J., Guo, B.J., Wang, Z.G., 2005. Precise Re-Os dating of molybdenite from the east Qinling molybdenum belt in central China and its geodynamic implications. In: J.W. Mao and F.P. Bierlein (Eds.), Proceedings of the Eighth Biennial SGA Meeting. Mineral Deposit Research: Meeting the Global Challenge. Springer-Verlag, Beijing, China, 777-780.

Li, Y.F., Mao, J.W., Bai, F.J., Li, J.P., He, Z.J., 2003. Re-Os isotopic dating of molybdenites in the Nannihu molybdenum (tungsten) ore field in the eastern Qinling and its geological significance. Geological Review 49, 292-304 (in Chinese with English abstract).

Li, Y.F., Mao, J.W., Liu, D.Y., Wang, Y.B., Wang, Z.L., Wang, Y.T., Li, X.F., Zhang, Z.H., Guo, B.J., 2006. SHRIMP zircon U-Pb and molybdenite Re-Os datings for the Leimengou porphyry molybdenum deposit, western Henan and its geological implication. Geological Review 52, 122-131 (in Chinese with English abstract).

Li, Z.K., 2013. Metallogenesis of the silver-lead-zinc deposits along the southern margin of the North China Craton, Ph. D. thesis, China University of Geosciences, Wuhan, 202 pp (in Chinese with English abstract).

Li, Z.K., Li, J.W., Chen, L., Zhang, S.X., Zheng, S., 2010. Occurrence of silver in the Shagou Ag-Pb-

766 Zn deposit, Luoning County, Henan Province: implications for mechanism of silver enrichment.
767 Earth Science 35, 621-636 (in Chinese with English abstract).
768 Li, Z.K., Li, J.W., Zhao, X.F., Zhou, M.F., Selby, D., Bi, S.J., Sui, J.X., Zhao, Z.J., 2013b. Crustal-
769 extension Ag-Pb-Zn veins in the Xiong'ershan district, southern North China craton: constraints
770 from the Shagou deposit. Econ. Geol. 108, 1703-1729.
771 Liu, Y.S., Gao, S., Hu, Z.C., Gao, C.G., Zong, K.Q., Wang, D.B., 2010. Continental and oceanic crust
772 recycling-induced melt-peridotite interactions in the Trans-North China Orogen: U-Pb dating, Hf
773 isotopes and trace elements in zircons from mantle xenoliths. J. Petrol. 51, 537-571.
774 Liu, Y.S., Zong, K.Q., Kelemen, P.B., Gao, S., 2008. Geochemistry and magmatic history of eclogites
775 and ultramafic rocks from the Chinese continental scientific drill hole: subduction and ultrahigh-
776 pressure metamorphism of lower crustal cumulates. Chem. Geol. 247, 133-153.
777 Longerich, H.P., Jackson, S.E., Günther, D., 1996. Laser ablation inductively coupled plasma mass
778 spectrometric transient signal data acquisition and analyte concentration calculation. J. Anal. Atom.
779 Spectrom. 11, 899-904.
780 Ludwig, K.R., 2003. User's manual for Isoplot 3.00: a geochronological toolkit for Microsoft Excel.
781 Ma, H.Y., Huang, C.Y., Ba, A.M., Li, H.L., Li, F.A., 2006. Metallogenic regularities and prospecting
782 criteria of Pb-Zn-Mo deposits in the south Ruyang Area. Geology and Prospecting 42, 17-22 (in
783 Chinese with English abstract).
784 Ma, H.Y., Lu, W.Q., Zhang, Y.Z., Li, H.L., Tian, X.Q., Ma, Y.F., 2007. Geological characters and
785 prospecting indication of Donggou Mo deposit in the Ruyang area, Henan. Geology and
786 Prospecting 43, 1-7 (in Chinese with English abstract).
787 Mao, J.W., Goldfarb, R.J., Zhang, Z.W., Xu, W.Y., Qiu, Y.M., Deng, J., 2002. Gold deposits in the
788 Xiaoqinling-Xiong'ershan region, Qinling Mountains, central China. Miner. Deposita 37, 306-325.
789 Mao, J.W., Pirajno, F., Xiang, J.F., Gao, J.J., Ye, H.S., Li, Y.F., Guo, B.J., 2011. Mesozoic
790 molybdenum deposits in the east Qinling-Dabie orogenic belt: characteristics and tectonic settings.
791 Ore Geol. Rev. 43, 264-293.
792 Mao, J.W., Xie, G.Q., Bierlein, F., Qu, W.J., Du, A.D., Ye, H.S., Pirajno, F., Li, H.M., Guo, B.J., Li,
793 Y.F., 2008. Tectonic implications from Re-Os dating of Mesozoic molybdenum deposits in the
794 East Qinling-Dabie orogenic belt. Geochim. Cosmochim. Ac. 72, 4607-4626.
795 Mao, J.W., Xie, G.Q., Pirajno, F., Ye, H.S., Wang, Y.B., Li, Y.F., Xiang, J.F., Zhao, H.J., 2010. Late

796 Jurassic-Early Cretaceous granitoid magmatism in Eastern Qinling, central-eastern China:
797 SHRIMP zircon U-Pb ages and tectonic implications. Aust. J. Earth Sci. 57, 51-78.
798 Mao, J.W., Ye, H.S., Wang, R.T., Dai, J.Z., Jian, W., Xiang, J.F., Zhou, K., 2009. Mineral deposit
799 model of Mesozoic porphyry Mo and vein-type Pb-Zn-Ag ore deposits in the eastern Qinling,
800 Central China and its implication for prospecting. Geological Bulletin of China 28, 72-79 (in
801 Chinese with English abstract).
802 Mao, J.W., Zheng, R.F., Ye, H.S., Gao, J.J., Chen, W., 2006. $^{40}Ar/^{39}$ Ar dating of fuchsite and sericite
803 from altered rocks close to ore veins in Shagou large-size Ag-Pb-Zn deposit of Xiong'ershan area,
804 western Henan Province, and its significance. Mineral Deposits 25, 359-368 (in Chinese with
805 English abstract).
806 McDougall, I., Harrison, T.M., 1999. Geochronology and thermochronology by the $^{40}Ar/^{39}Ar$ method.
807 Oxford University Press, Oxford, 269 pp.
808 Meffre, S., Large, R.R., Scott, R., Woodhead, J., Chang, Z., Gilbert, S.E., Danyushevsky, L.V.,
809 Maslennikov, V., Hergt, J.M., 2008. Age and pyrite Pb-isotopic composition of the giant Sukhoi
810 Log sediment-hosted gold deposit, Russia. Geochim. Cosmochim. Ac. 72, 2377-2391.
811 Morey, A.A., Tomkins, A.G., Bierlein, F.P., Weinberg, R.F., Davidson, G.J., 2008. Bimodal
812 distribution of gold in pyrite and arsenopyrite: examples from the Archean Boorara and Bardoc
813 shear systems, Yilgarn Craton, Western Australia. Econ. Geol. 103, 599-614.
814 Peng, P., Zhai, M., Ernst, R.E., Guo, J., Liu, F., Hu, B., 2008. A 1.78 Ga large igneous province in the
815 North China craton: The Xiong'er Volcanic Province and the North China dyke swarm. Lithos 101,
816 260-280.
817 Pirajno, F., Zhou, T., 2015. Intracontinental porphyry and porphyry-skarn mineral systems in Eastern
818 China: scrutiny of a special case "Made-in-China". Econ. Geol. 110, 603-629.
819 Qi, J.P., Chen, Y.J., Ni, P., Lai, Y., Ding, J.Y., Song, Y.W., Tang, G.J., 2007. Fluid inclusion
820 constraints on the origin of the Lengshuibeigou Pb-Zn-Ag deposit, Henan province. Acta Petrol.
821 Sin. 23, 2119-2130 (in Chinese with English abstract).
822 Qi, Y., 2014. Petrogenesis of Laojunshan and Taishanmiao granite plutons in Eastern Qinling, central
823 China, Master thesis, University of Science and Technology of China, Hefei, 73 pp.
824 Reich, M., Deditius, A., Chryssoulis, S., Li, J., Ma, C., Parada, M.A., Barra, F., Mittermayr, F., 2013.
825 Pyrite as a record of hydrothermal fluid evolution in a porphyry copper system: A SIMS/EMPA

826 trace element study. Geochim. Cosmochim. Ac. 104, 42-62.
827 Ren, J., Tamaki, K., Li, S., Junxia, Z., 2002. Late Mesozoic and Cenozoic rifting and its dynamic
828 setting in Eastern China and adjacent areas. Tectonophysics 344, 175-205.
829 Renne, P.R., Deino, A.L., Hames, W.E., Heizler, M.T., Hemming, S.R., Hodges, K.V., Koppers, A.A.,
830 Mark, D.F., Morgan, L.E., Phillips, D., 2009. Data reporting norms for $^{40}Ar/^{39}Ar$ geochronology.
831 Quat. Geochronol. 4, 346-352.
832 Richards, J.P., 2003. Tectono-magmatic precursors for porphyry Cu-(Mo-Au) deposit formation. Econ.
833 Geol. 98, 1515-1533.
834 Schütte, P., Chiaradia, M., Barra, F., Villagómez, D., Beate, B., 2012. Metallogenic features of
835 Miocene porphyry Cu and porphyry-related mineral deposits in Ecuador revealed by Re-Os,
836 $^{40}Ar/^{39}Ar$, and U-Pb geochronology. Miner. Deposita 47, 383-410.
837 Seedorff, E., Dilles, J.H., Proffett, J.M., Einaudi, M.T., Zurcher, L., Stavast, W., Johnson, D.A., Barton,
838 M.D., 2005. Porphyry deposits: characteristics and origin of hypogene features. Economic Geology
839 100th Anniversary Volume, 251-298.
840 Selby, D., Creaser, R.A., 2001. Re-Os geochronology and systematics in molybdenite from the Endako
841 porphyry molybdenum deposit, British Columbia, Canada. Econ. Geol. 96, 197-204.
842 Selby, D., Creaser, R.A., Hart, C.J., Rombach, C.S., Thompson, J.F., Smith, M.T., Bakke, A.A.,
843 Goldfarb, R.J., 2002. Absolute timing of sulfide and gold mineralization: A comparison of Re-Os
844 molybdenite and Ar-Ar mica methods from the Tintina Gold Belt, Alaska. Geology 30, 791-794.
845 Selby, D., Creaser, R.A., Stein, H.J., Markey, R.J., Hannah, J.L., 2007. Assessment of the 187 Re
846 decay constant by cross calibration of Re-Os molybdenite and U-Pb zircon chronometers in
847 magmatic ore systems. Geochim. Cosmochim. Ac. 71, 1999-2013.
848 Shi, Q.Z., Wei, X.D., Li, M.L., Pang, J.Q., 2004. Nappe and extensional detachment structures in north
849 side of East Qinling, Henan. Geological Publishing House, Beijing, 204 pp (in Chinese with
850 English abstract).
851 Sillitoe, R.H., 1973. The tops and bottoms of porphyry copper deposits. Econ. Geol. 68, 799-815.
852 Sillitoe, R.H., 2000. Gold-rich porphyry deposits, Descriptive and genetic models and their role in
853 exploration and discovery. In: Hagemann SG, Brown PE (eds.) Gold in 2000. Rev Econ Geol, 315-
854 345.
855 Sillitoe, R.H., 2010. Porphyry copper systems. Econ. Geol. 105, 3-41.

856 Smoliar, M.I., Walker, R.J., Morgan, J.W., 1996. Re-Os ages of group IIA, IIIA, IVA, and IVB iron
857 meteorites. Science 271, 1099.
858 Steadman, J.A., Large, R.R., Meffre, S., Bull, S.W., 2013. Age, origin and significance of nodular
859 sulfides in 2680 Ma carbonaceous black shale of the Eastern Goldfields Superterrane, Yilgarn
860 Craton, Western Australia. Precambrian Res. 230, 227-247.
861 Steiger, R.H., Jäger, E., 1977. Subcommission on geochronology: convention on the use of decay
862 constants in geo-and cosmochronology. Earth Planet. Sc. Lett. 36, 359-362.
863 Stein, H.J., Markey, R.J., Morgan, J.W., Hannah, J.L., Scherstén, A., 2001. The remarkable Re-Os
864 chronometer in molybdenite: how and why it works. Terra Nova 13, 479-486.
865 Suzuki, K., Shimizu, H., Masuda, A., 1996. Re-Os dating of molybdenites from ore deposits in Japan:
866 Implication for the closure temperature of the Re Os system for molybdenite and the cooling
867 history of molybdenum ore deposits. Geochim. Cosmochim. Ac. 60, 3151-3159.
868 Wang, C.M., He, X.Y., Yan, C.H., Lü, W.D., Sun, W.Z., 2013. Ore geology, and H, O, S, Pb, Ar
869 isotopic constraints on the genesis of the Lengshuibeigou Pb-Zn-Ag deposit, China. Geosci. J. 17,
870 197-210.
871 Wang, S.S., 1983. Age determinations of ^{40}Ar-^{40}K, ^{40}Ar-^{39}Ar and radiogenic ^{40}Ar released
872 characteristics on K-Ar geostandards of China. Scientia Geologica Sinica 4, 315-323.
873 Wang, Z.G., Zhang, L.X., 1999. Metamorphic core complex in Xiong'ershan and the advances in
874 prospecting. Geological Exploration for Non-ferrous Metals 8, 388-392 (in Chinese with English
875 abstract).
876 Wilson, S.A., Ridley, W.I., Koenig, A.E., 2002. Development of sulfide calibration standards for the
877 laser ablation inductively-coupled plasma mass spectrometry technique. J. Anal. Atom. Spectrom.
878 17, 406-409.
879 Woodhead, J., 2002. A simple method for obtaining highly accurate Pb isotope data by MC-ICP-MS. J.
880 Anal. Atom. Spectrom. 17, 1381-1385.
881 Woodhead, J., Hergt, J., Meffre, S., Large, R.R., Danyushevsky, L., Gilbert, S., 2009. In situ Pb-
882 isotope analysis of pyrite by laser ablation (multi-collector and quadrupole) ICPMS. Chem. Geol.
883 262, 344-354.
884 Wu, F.Y., Lin, J.Q., Wilde, S.A., Zhang, X.O., Yang, J.H., 2005. Nature and significance of the Early
885 Cretaceous giant igneous event in eastern China. Earth Planet. Sc. Lett. 233, 103-119.

886 Wu, Y.B., Zheng, Y.F., 2004. Genesis of zircon and its constraints on interpretation of U-Pb age.
887 Chinese Sci. Bull. 49, 1554-1569.
888 Xu, X.S., Griffin, W.L., Ma, X., O'Reilly, S.Y., He, Z.Y., Zhang, C.L., 2009. The Taihua group on the
889 southern margin of the North China craton: further insights from U-Pb ages and Hf isotope
890 compositions of zircons. Miner. Petrol. 97, 43-59.
891 Yan, C.H., 2004. Study on inner structure of Pb-Zn-Ag mineralization system in eastern Qinling.
892 Geology Publishing House, Beijing, 144 pp (in Chinese with English abstract).
893 Yan, J.S., Wang, M.S., Yang, J.C., Xu, Y.X., 2000. Tectonic evolution of the Machaoying fault zone in
894 western Henan and its relationship with Au polymetallic mineralization. Regional Geology of
895 China 19, 166-171 (in Chinese with English abstract).
896 Yang, Y.F., Chen, Y.J., Pirajno, F., Li, N., Pirajno, F., 2015. Evolution of ore fluids in the Donggou
897 giant porphyry Mo system, East Qinling, China, a new type of porphyry Mo deposit: Evidence
898 from fluid inclusion and H-O isotope systematics. Ore Geol. Rev. 65, 148-164.
899 Yang, Y.F., Li, N., Wang, L.J., 2011. Fluid inclusion study of the Donggou porphyry Mo deposit,
900 Henan Province. Acta Petrol. Sin. 27, 1453-1466 (in Chinese with English abstract).
901 Yang, Z.Y., Cheng, Y.Q., Wang, H.Z., 1986. The geology of China. Clarendon Press Oxford, New
902 York, 306 pp.
903 Yao, J.M., Chen, Y.J., Zhao, T.P., Li, X.H., Yuan, Z.L., 2010. Fluid inclusions and Rb-Sr isotopic
904 dating of the Wangpingxigou Pb-Zn deposit, Henan Province, China. Mineral Deposits 29, 535-
905 536 (in Chinese with English abstract).
906 Yao, J.M., Zhao, T.P., Wei, Q.G., Yuan, Z.L., 2008. Fluid inclusion features and genetic type of the
907 Wangpingxigou Pb-Zn deposit, Henan Province. Acta Petrol. Sin. 24, 2113-2123 (in Chinese with
908 English abstract).
909 Ye, H.S., 2006. The Mesozoic tectonic evolution and Pb-Zn-Ag metallogeny in the south margin of
910 North China Craton, Ph. D. thesis, China University of Geosciences, Beijing, 217 pp (in Chinese
911 with English abstract).
912 Ye, H.S., Mao, J.W., Li, Y.F., Guo, B.J., Zhang, C.Q., Liu, W.J., Yan, Q.R., 2006. SHRIMP Zircon U-
913 Pb and molybdenite Re-Os dating for the superlarge Donggou porphyry Mo deposit in East Qinling,
914 China, and its geological implication. Acta Geol. Sin. 80, 1078-1088 (in Chinese with English
915 abstract).

916 Ye, H.S., Mao, J.W., Xu, L.G., Gao, J.J., Xie, G.Q., Li, X.Q., He, C.F., 2008. SHRIMP zircon U-Pb
917 dating and geochemistry of the Taishanmiao aluminous A-type granite in western Henan Province.
918 Geological Review 54, 699-711 (in Chinese with English abstract).
919 Zhai, M.G., 2010. Tectonic evolution and metallogenesis of North China Craton. Mineral Deposits 29,
920 24-36 (in Chinese with English abstract).
921 Zhang, J.J., Zheng, Y.D., 1999. The multiphase extension and their ages of the Xiaoqinling
922 metamorphic core complex. Acta Geol. Sin. 73, 139-147 (in Chinese with English abstract).
923 Zhao, G.C., Cawood, P.A., Wilde, S.A., Sun, M., Lu, L.Z., 2000. Metamorphism of basement rocks in
924 the Central Zone of the North China Craton: implications for Paleoproterozoic tectonic evolution.
925 Precambrian Res. 103, 55-88.
926 Zhao, G.C., He, Y.H., Sun, M., 2009. The Xiong'er volcanic belt at the southern margin of the North
927 China Craton: Petrographic and geochemical evidence for its outboard position in the Paleo-
928 Mesoproterozoic Columbia Supercontinent. Gondwana Res. 17, 145-152.
929 Zhao, G.C., Wilde, S.A., Cawood, P.A., Sun, M., 2001. Archean blocks and their boundaries in the
930 North China Craton: lithological, geochemical, structural and P-T path constraints and tectonic
931 evolution. Precambrian Res. 107, 45-73.
932 Zhao, T.P., Zhai, M.G., Xia, B., Li, H.M., Zhang, Y.X., Wan, Y.S., 2004. Zircon U-Pb SHRIMP dating
933 for the volcanic rocks of the Xiong'er Group: Constraints on the initial formation age of the cover
934 of the North China Craton. Chinese Sci. Bull. 49, 2495-2502.
935 Zhao, T.P., Zhou, M.F., Zhai, M., Xia, B., 2002. Paleoproterozoic rift-related volcanism of the
936 Xiong'er Group, North China Craton: implications for the breakup of Columbia. Int. Geol. Rev. 44,
937 336-351.
938 Zhou, H.W., Zhong, Z.Q., Ling, W.L., 1998. Sm-Nd isochron for the amphibolites within Taihua
939 complex from Xiaoqinling area, western Henan and its geological implications. Geochimica 27,
940 367-372 (in Chinese with English abstract).
941 Zhu, R.X., Yang, J.H., Wu, F.Y., 2012. Timing of destruction of the North China Craton. Lithos 149,
942 51-60.
943
944

945 ## Figure and table captions

946 **Fig. 1** Geological map showing major mineral districts along the southern margin of the NCC
947 (modified from Mao et al., 2010; Li et al., 2013b). The insert map shows the tectonic location of the
948 southern NCC in Eastern China. Abbreviations: TNCO: Trans-North China Orogen, MCC:
949 metamorphic core complex.

950 **Fig. 2** Geological map of the Fudian ore field showing the locations of the Donggou porphyry Mo
951 deposit and surrounding Pb-Zn-Ag vein deposits (simplified from Bureau of Geological Exploration
952 and Mineral Development of Henan Province, 1992). Abreviations: F1: Yangping-Wangping fault; F2:
953 Jincun-Fudian fault. For map location see Fig. 1.

954 **Fig. 3** Geological map of the Donggou porphyry Mo deposit (after Ma et al., 2007). For map location
955 see Fig. 2.

956 **Fig. 4** Representative cross sections of the Donggou porphyry Mo deposit, showing distribution and
957 morphology of ore bodies (after Ma et al., 2007). For map location see Fig. 3.

958 **Fig. 5** Photographs showing occurrences and structures of ores at Donggou. (a) The contact zone
959 between the mineralized granite porphyry and the andesite of the Xiong'er Group. Note the
960 molybdenite disseminations both in the granite porphyry and the andesite. (b) Coarse-grained
961 molybdenite disseminated in the granite porphyry. Potassic alteration is well developed in the granite
962 porphyry. (c) Hydrothermal vein consisting of coarse-grained K-feldspar and molybdenite filling the
963 fracture of the andesite. (d) Both the K-feldspar – molybdenite vein and quartz – molybdenite vein
964 cutting the andesite. Note that the K-feldspar – molybdenite veins may be overprinted by a quartz –
965 molybdenite vein. (e) Pyrite-sphalerite-molybdenite vein filling the fracture of the Mo-mineralized
966 andesite. (f) Polymetallic vein cutting the andesite. The sulfide minerals in the vein include pyrite,
967 molybdenite, and galena. Abbreviations: Mo: molybdenite, Kfs: K-feldspar, Qz: quartz, Py: pyrite, Sp:
968 sphalerite, Gn: galena.

969 **Fig. 6** Transmitted-light (a) and reflected-light (b-f) photomicrographs illustrating the mineralogy and
970 textures of the granite porphyry and sulfide ores at Donggou, respectively. (a) Perthite and quartz
971 phenocrysts in the granite porphyry. (b) Stage D1 molybdenite aggregates intergrown with K-feldspar
972 and quartz. (c) Coarse-grained stage D2 molybdenite and quartz vein cutting the potassic zone. (d)
973 Stage D3 chalcopyrite and galena filling microfractures in coarse-grained, euhedral pyrite. (e) Stage D3

974 sphalerite intergrown with chalcopyrite and galena cutting massive quartz. (f) Stage D3 galena
975 replacing sphalerite. Abbreviations: Pth: Perthite, Ccp: chalcopyrite, other abbreviations as in Figure 5.
976 **Fig. 7** Paragenetic sequence of the Donggou deposit.
977 **Fig. 8** Photographs showing occurrences and structures of the ores at Sanyuangou. (a) Sulfide veinlets
978 penetrating quartz and ankerite in a steeply-dipping fault zone cutting the quartz diorite. (b) Quartz-
979 galena-sphalerite vein as fracture infillings in the quartz diorite. (c) Coarse-grained sphalerite and
980 galena aggregates in quartz diorite. (d) Massive sphalerite and galena ores replacing quartz diorite
981 breccias. (e) Massive galena-dominated ores. (f) Textural relationship of a vein consisting of the outer
982 siderite and ankerite, the intermediate galena and quartz, and the inner coarse-grained calcite.
983 Abbreviations: Sd: siderite, Ank: ankerite, Cal: calcite; other abbreviations as in Figure 5.
984 **Fig. 9** Reflected-light (a-d) and transmitted-light (e-f) photomicrographs illustrating the mineralogy
985 and textures of sulfide ores and associated alteration at Sanyuangou. (a) Stage S1 pyrite was fractured
986 and filled by paragenetically late chalcopyrite, sphalerite, and galena. (b) Stage S2 bornite and
987 sphalerite replacing pyrite; all of which were altered by galena. Note that tetrahedrite is intergrown
988 with bornite. (c) Stage S2 covellite forming selvages around foam-like pyrite; chalcopyrite forming
989 inclusions in sphalerite. (d) Stage S2 sphalerite with chalcopyrite inclusions filled and replaced by
990 galena. (e) Stage S3 calcite intergrown with coarse-grained quartz. (f) Sericite aggregates intergrown
991 associated with Pb-Zn sulfide mineralization. Abbreviations: Ccp: chalcopyrite, Bn: bornite, Ttr:
992 tetrahedrite, Cv: covellite, Cal: calcite, Ser: sericite; other abbreviations as in Figure 5.
993 **Fig. 10** Paragenetic sequence of the Sanyuangou deposit.
994 **Fig. 11** U-Pb concordia diagrams of zircons from the Donggou granite porphyry (a), the Sanyuangou
995 quartz diorite (b), and the Wangpingxigou quartz monzonite (c).
996 **Fig. 12** $^{40}Ar/^{39}Ar$ age spectra (a) and inverse isochron (b) of stage S2 sericite from Sanyuangou.
997 **Fig. 13** Diagrams showing the concentrations of selected trace elements for pyrite from Donggou and
998 Sanyuangou. Red dotted line indicates the detection limits of the trace elements.
999 **Fig. 14** Correlation between Co and Ni for pyrite from Donggou and Sanyuangou. The shadow areas
1000 show the average detection limit of the trace elements.
1001 **Fig. 15** Thorogenic (a) and uranogenic (b) lead isotopic diagrams for pyrites from Donggou and
1002 Sanyuangou. The dotted lines are trend lines for the spots. NHRL shows the North hemisphere
1003 reference line (Hart, 1984).

1004

1005 **Table 1** Re-Os isotope data of molybdenite from the Donggou deposit.

1006 **Table 2** $^{40}Ar/^{39}Ar$ analytical results of stage S2 sericite from Sanyuangou.

1007 **Table 3** Lead isotopic compositions of pyrite from Donggou and Sanyuangou

1008 **Appendix 1** Laser ablation ICP-MS zircon U-Pb dating results for the Donggou granite porphyry,

1009 Sanyuangou quartz diorite, and Wangpingxigou quartz monzonite.

1010 **Appendix 2** Laser ablation ICP-MS spot analyses of pyrite from Donggou and Sanyuangou

1011

Li et al. Figure 1

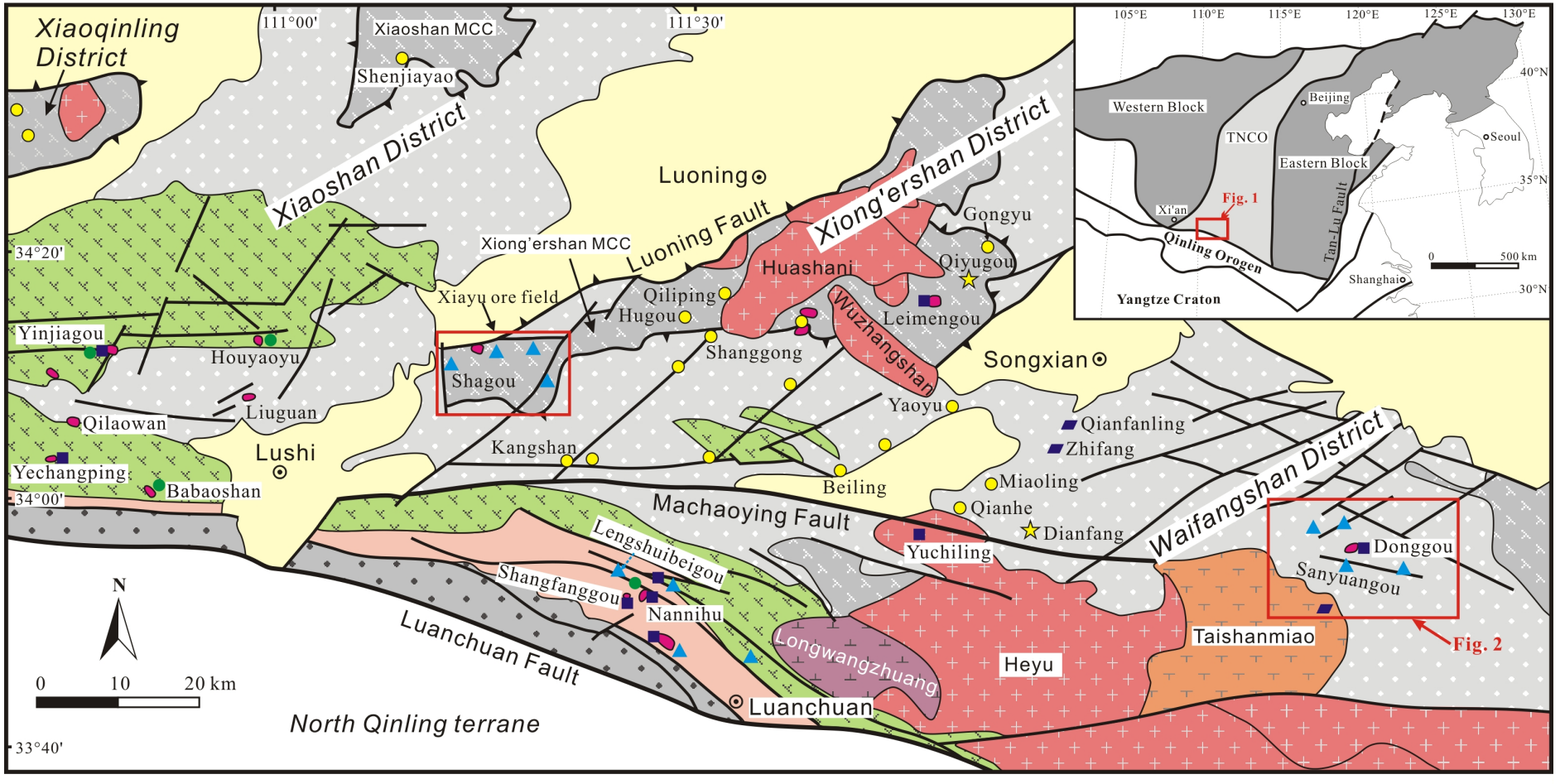

Li et al. Figure 2

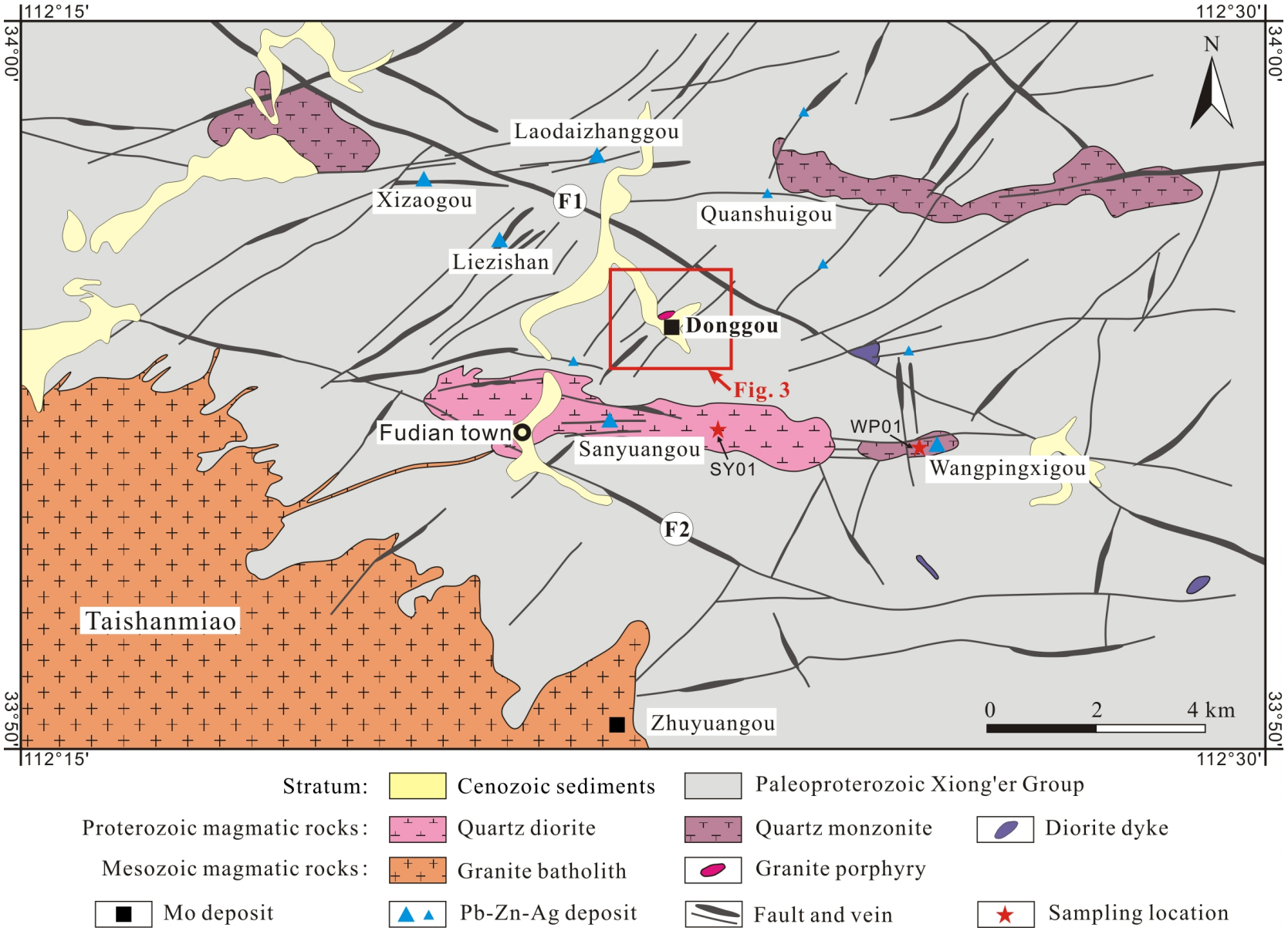

Li et al. Figure 3

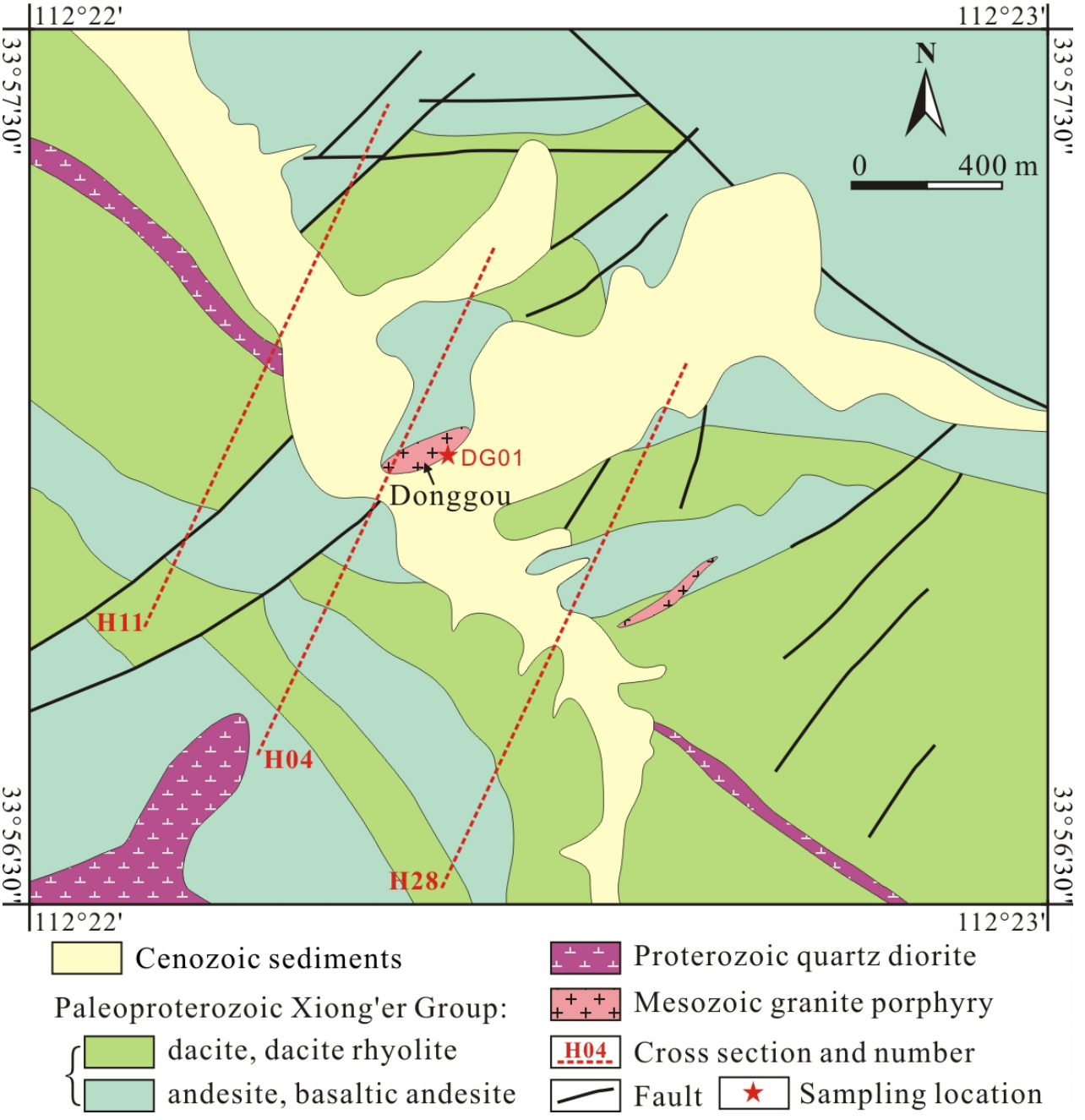

Li et al. Figure 4

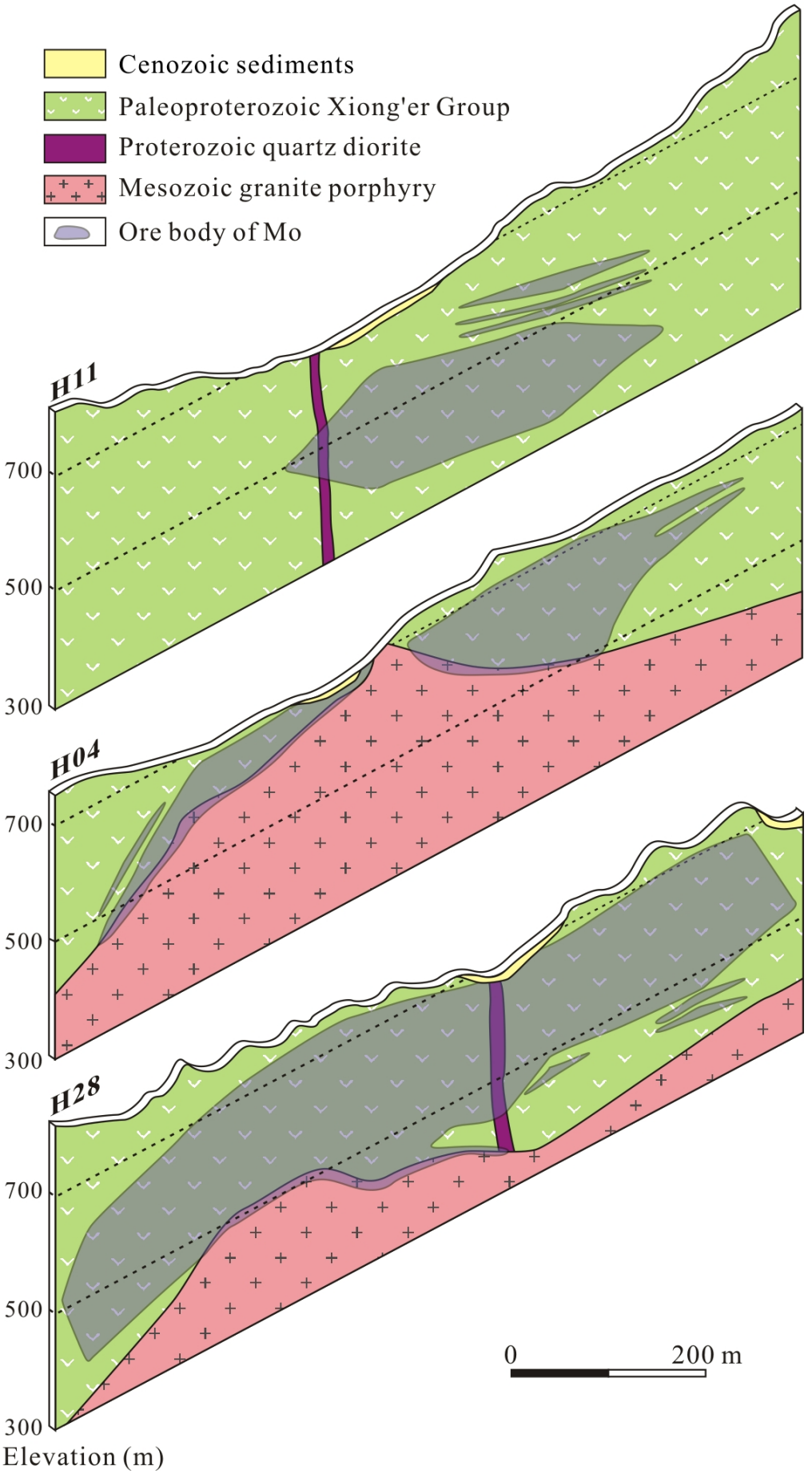

Li et al. Figure 5

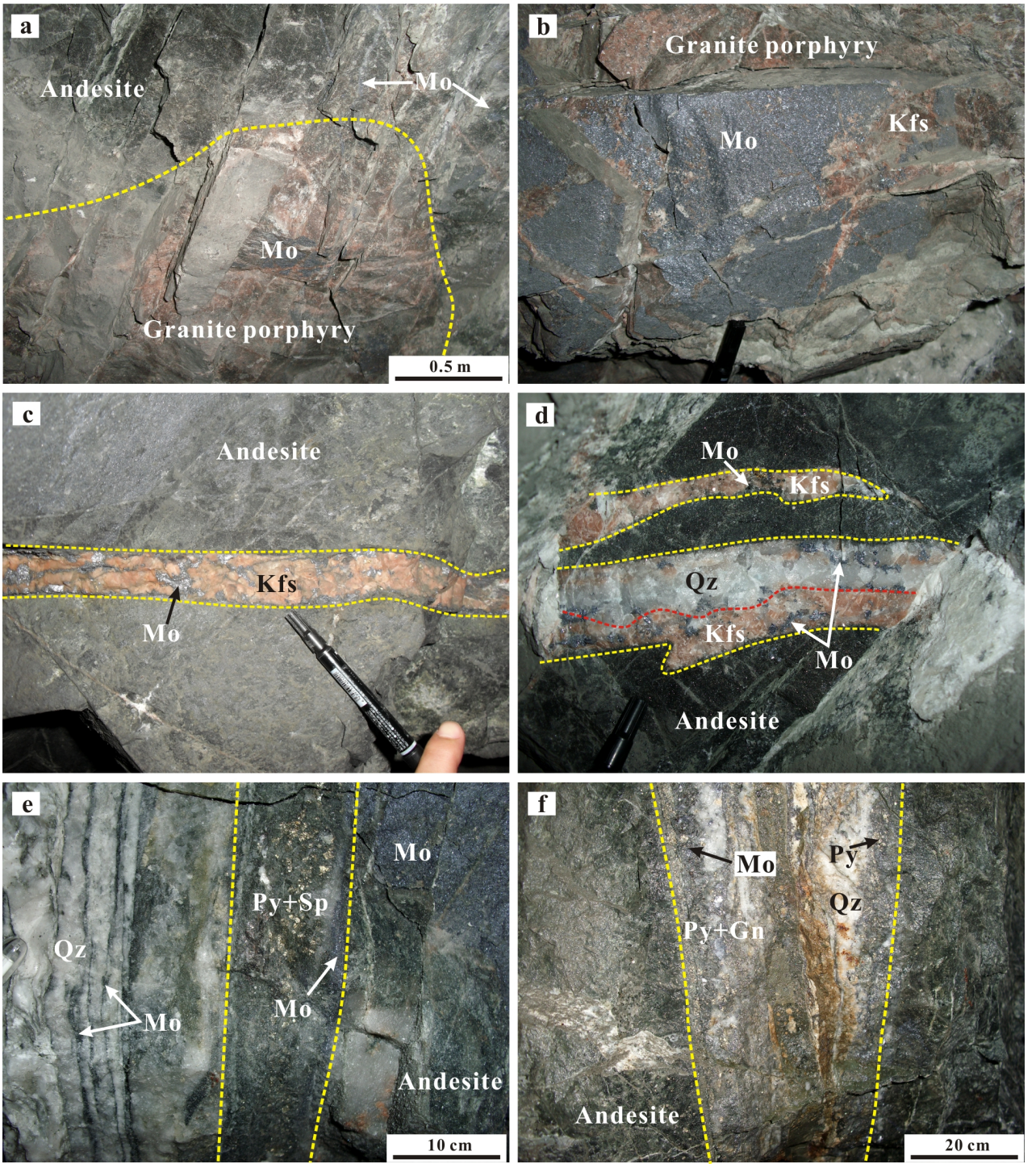

Li et al. Figure 6

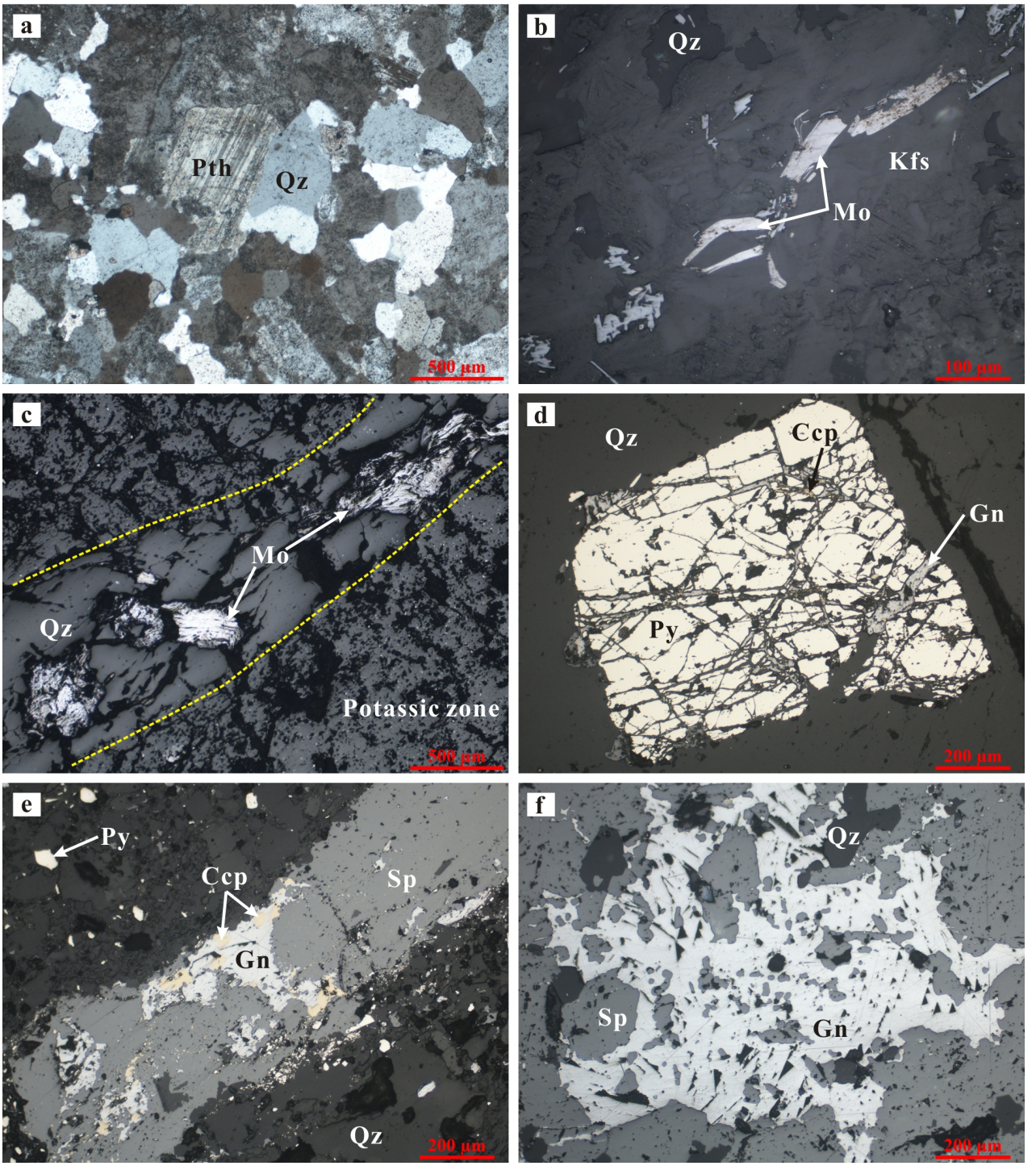

Li et al. Figure 7

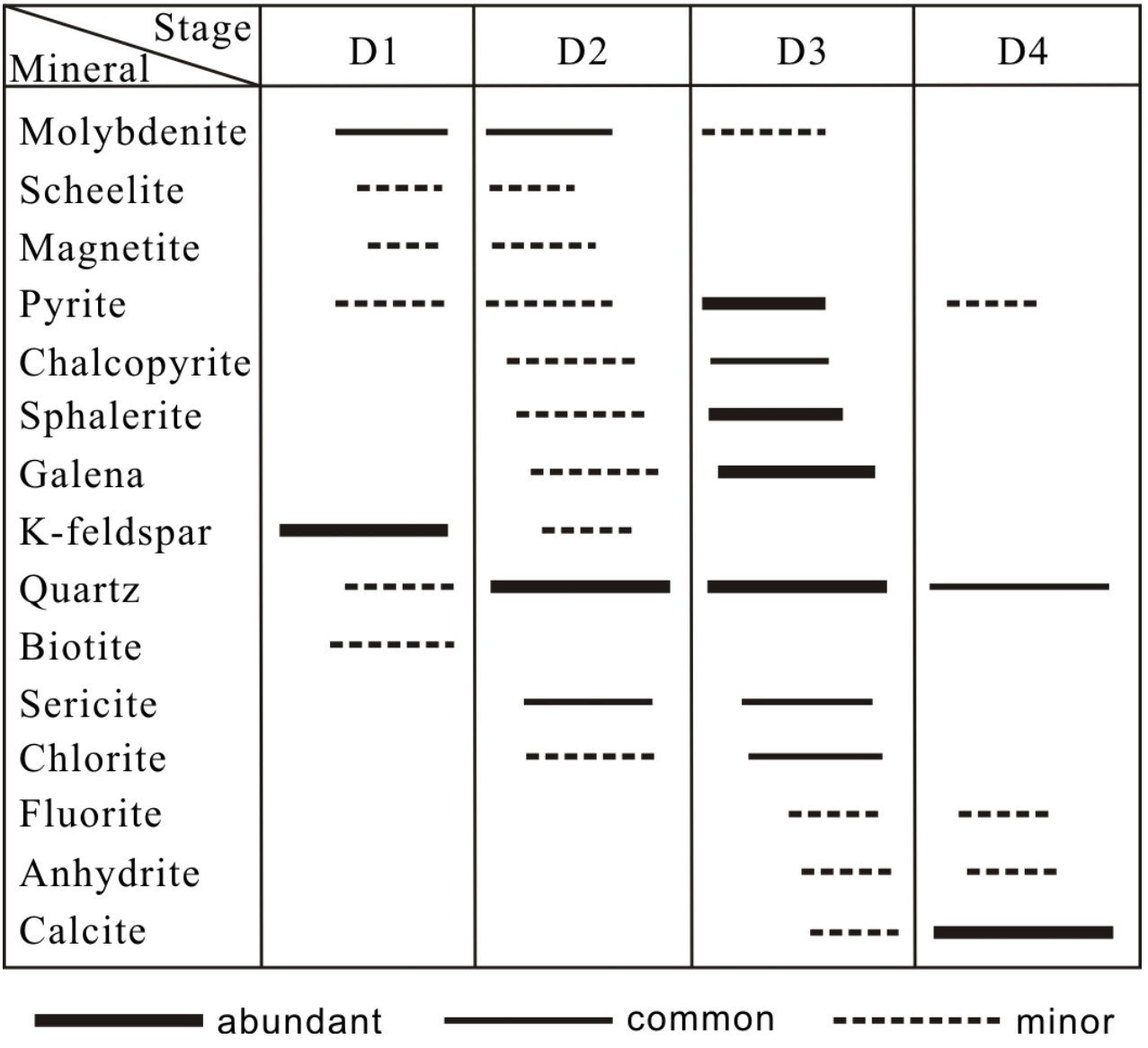

Li et al. Figure 8

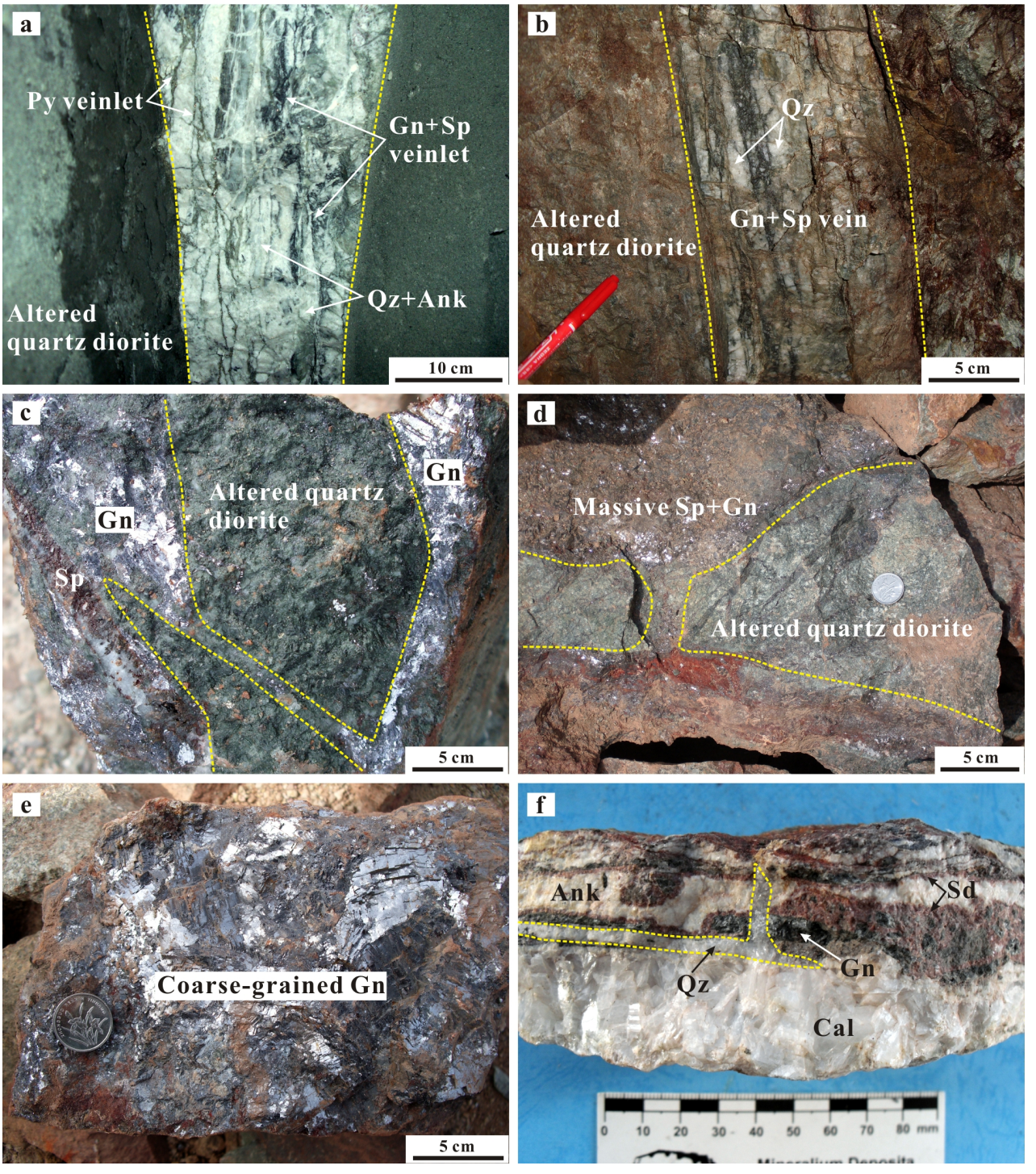

Li et al. Figure 9

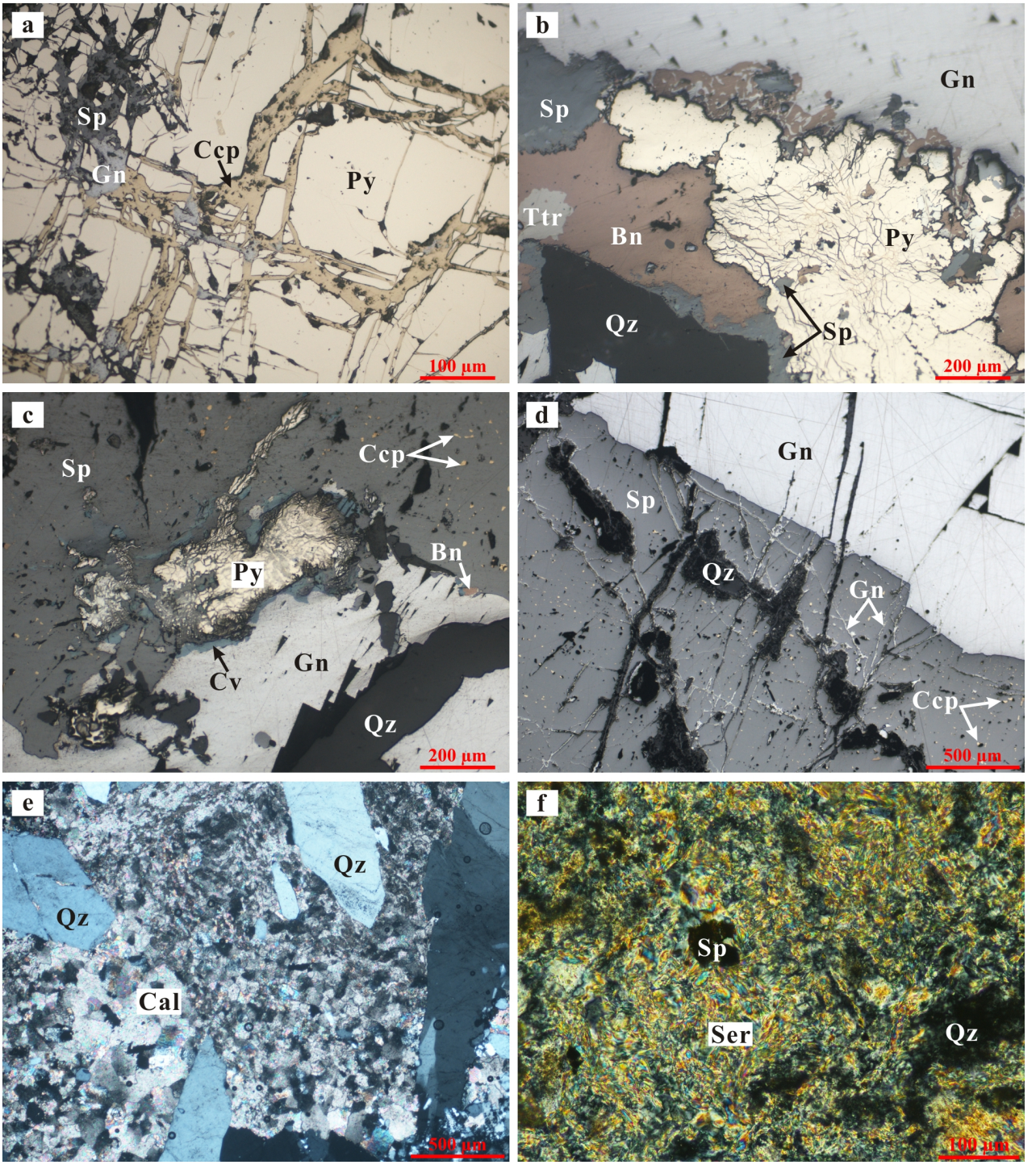

Li et al. Figure 10

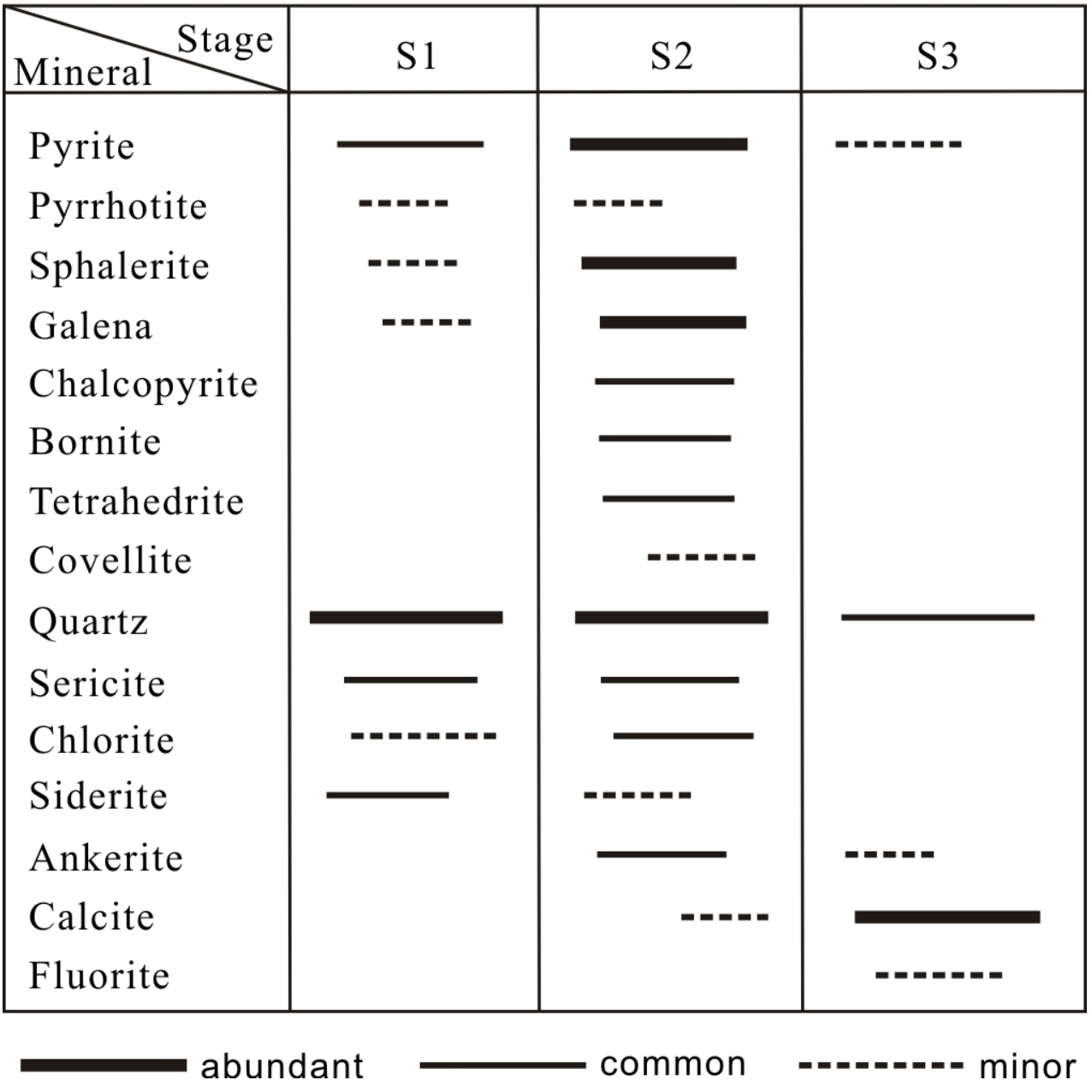

Li et al. Figure 11

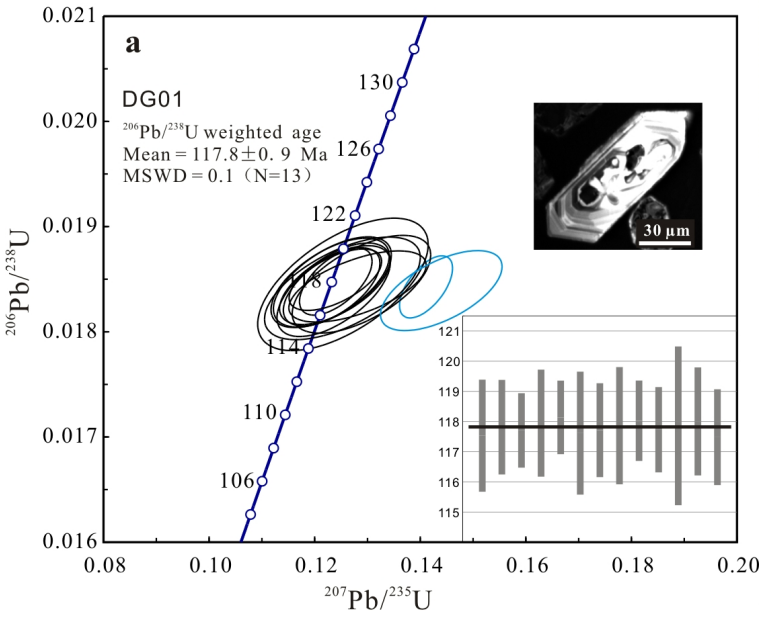

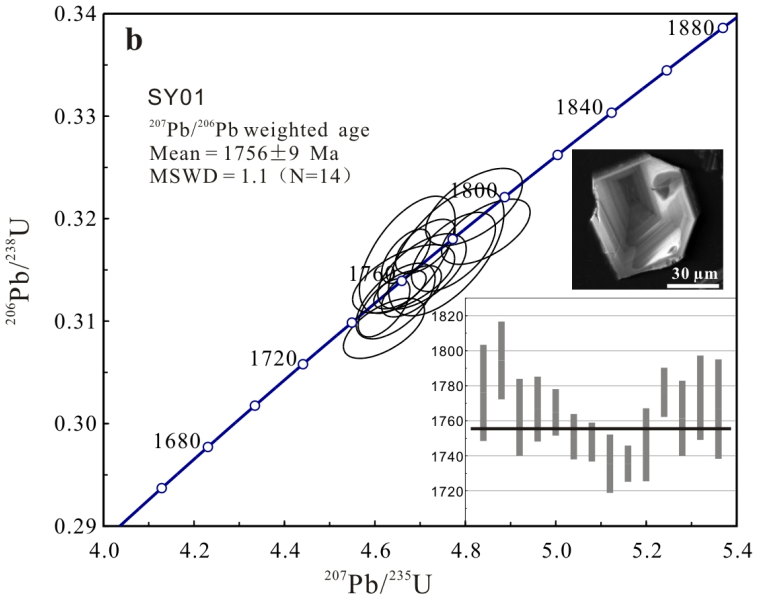

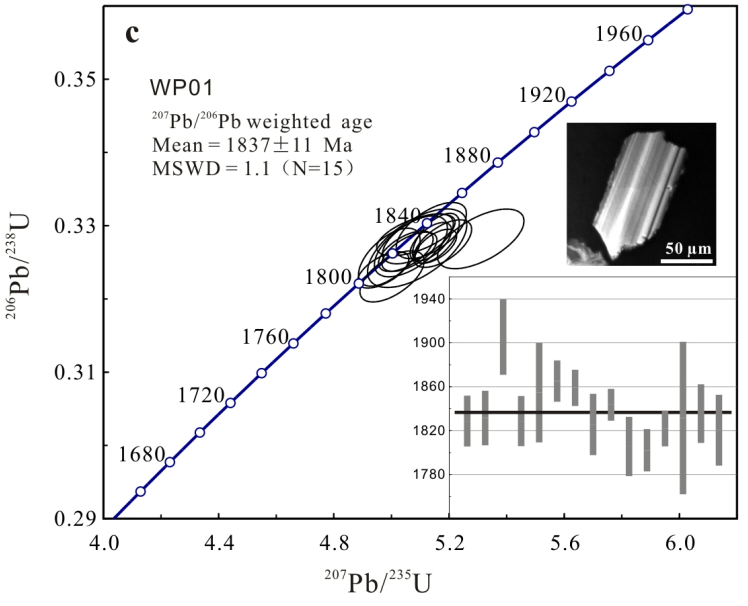

Li et al. Figure 12

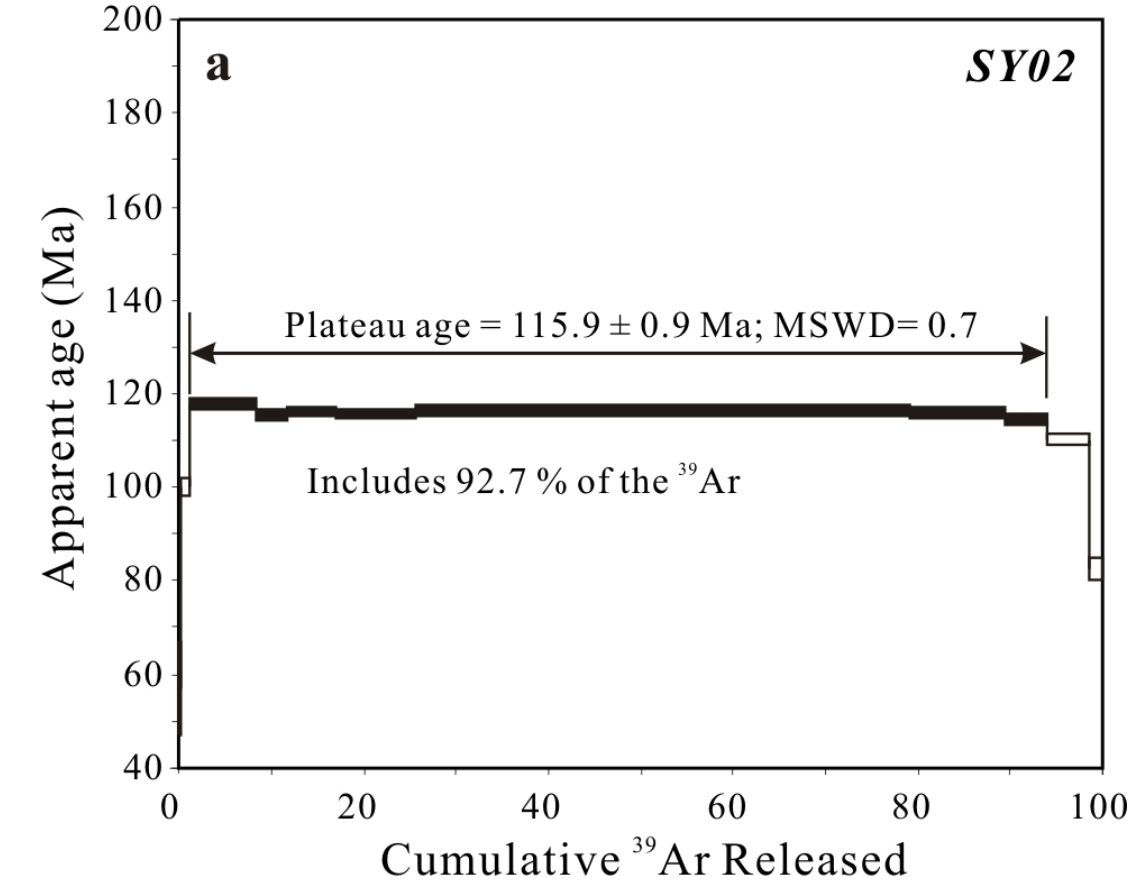

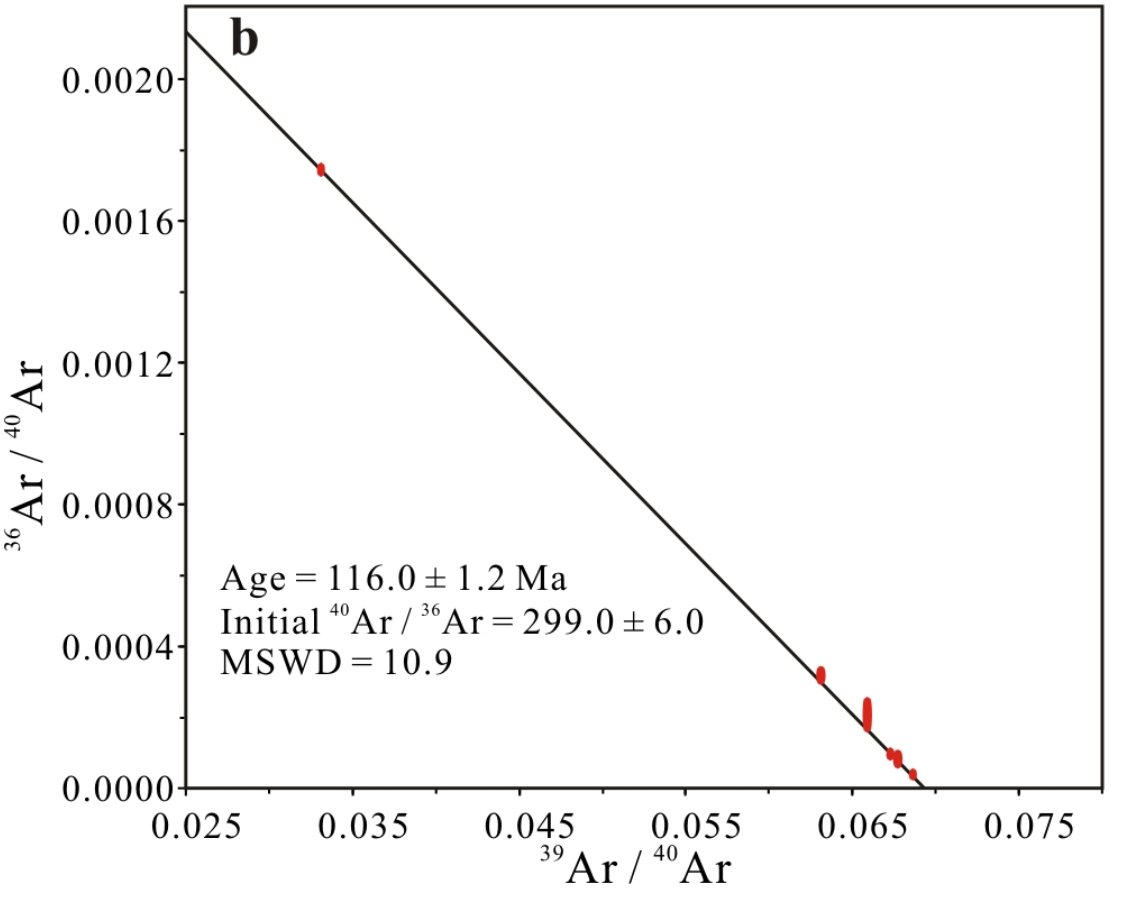

Li et al. Figure 13

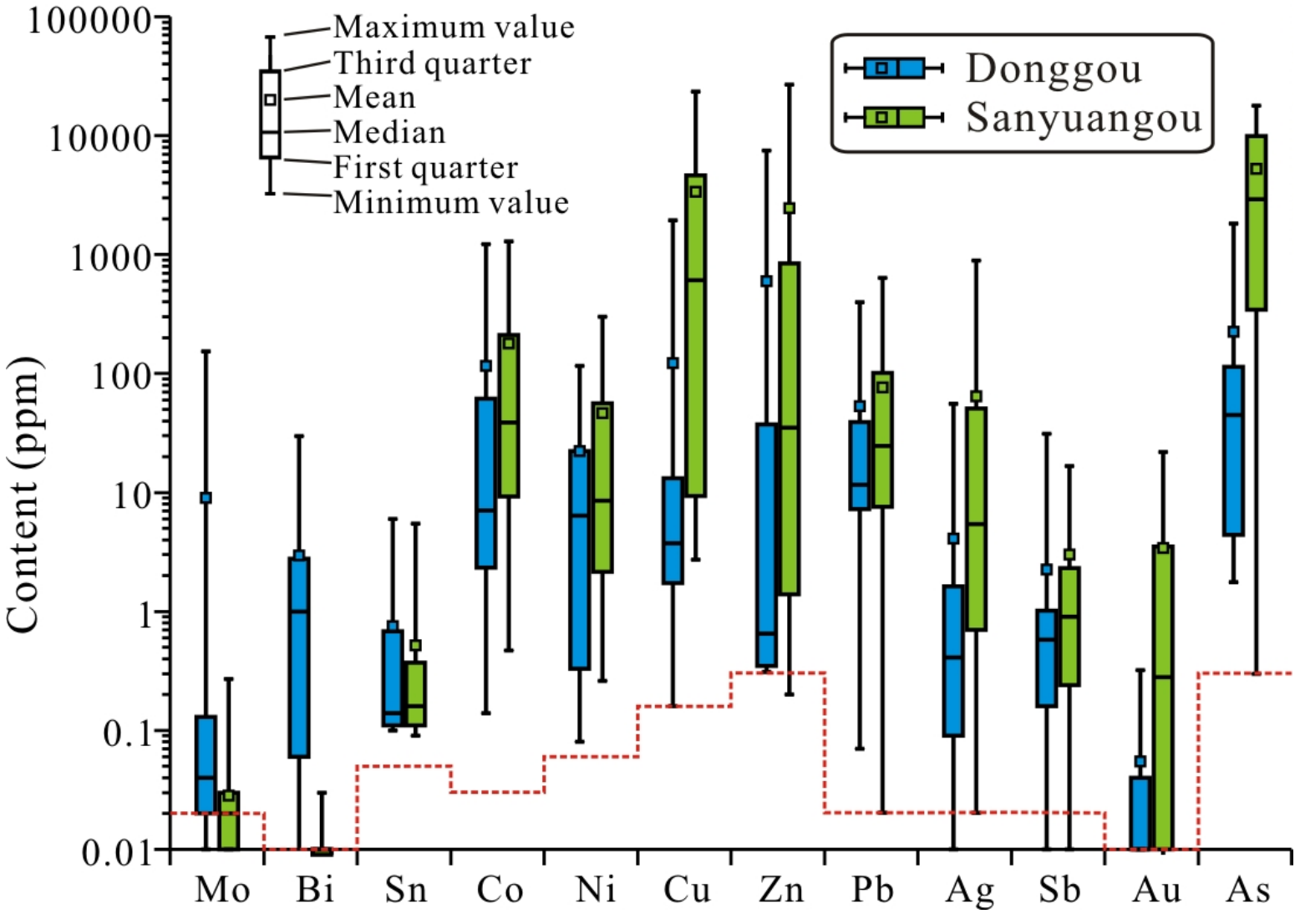

Li et al. Figure 14

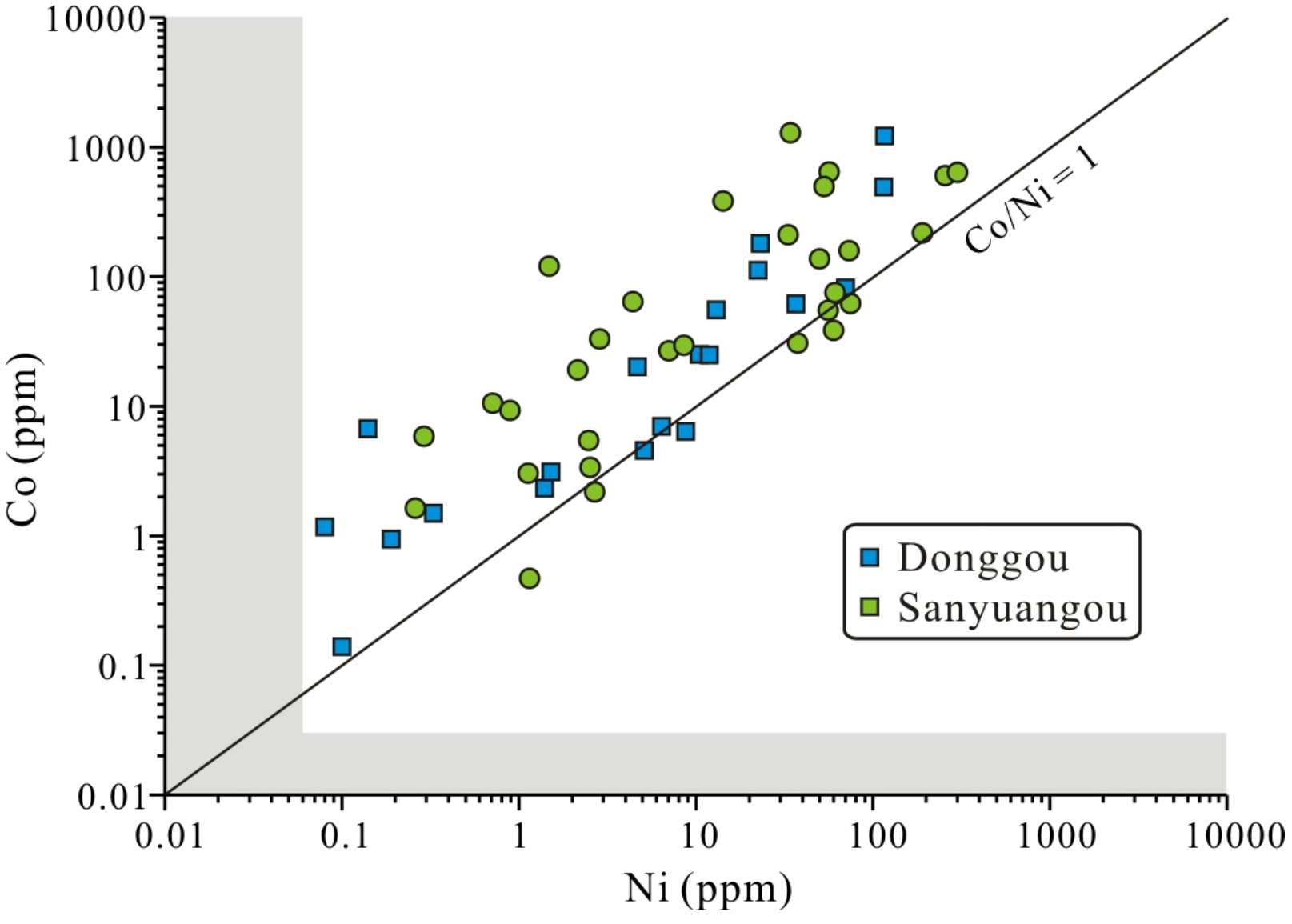

Li et al. Figure 15

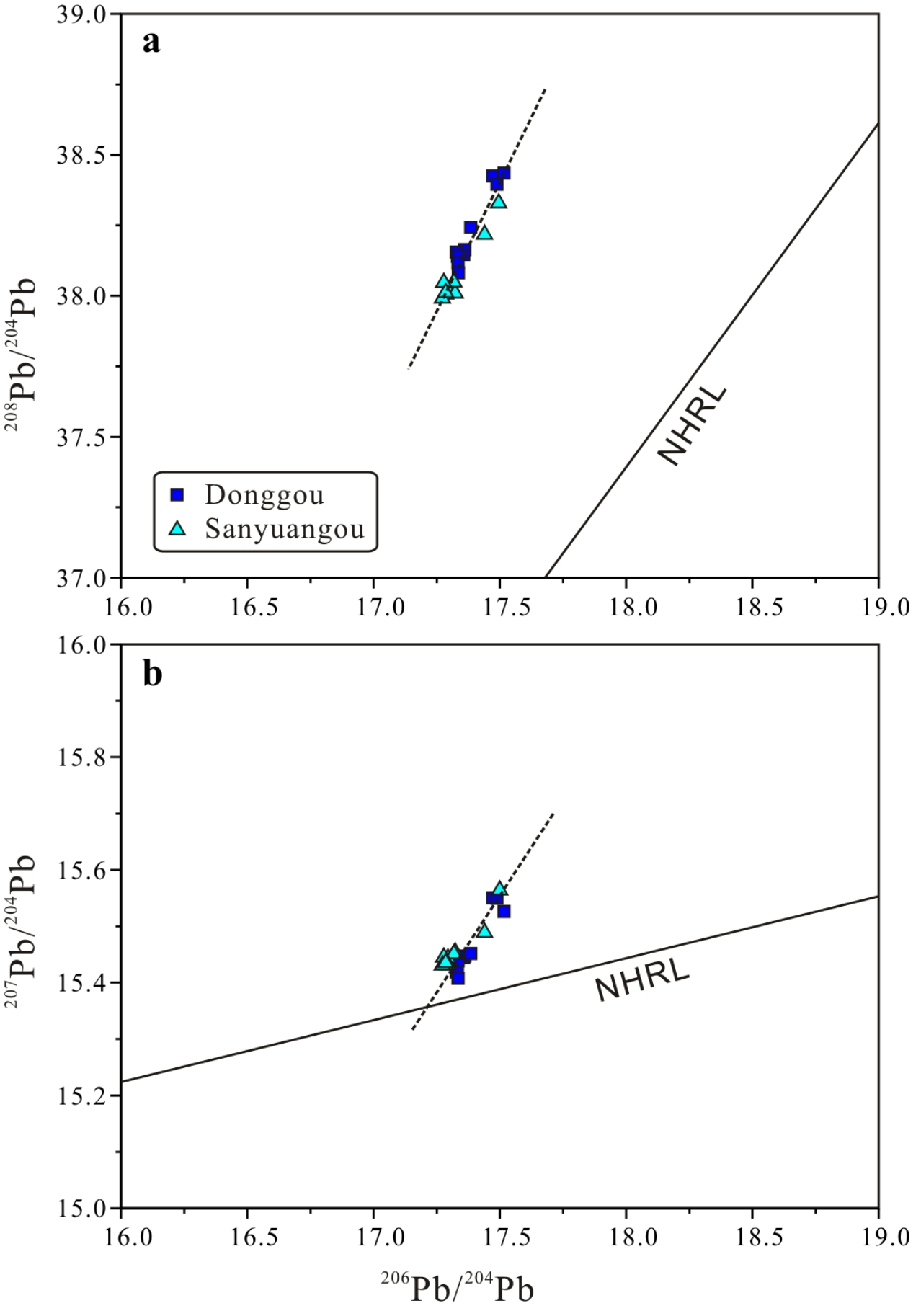

Table 1 Re-Os isotopic data of molybdenite from the Donggou deposit

Sample No.	Location	Weight (mg)	Re (ppm)	±	^{187}Re (ppm)	±	^{187}Os (ppb)	±	Age (Ma)	±[a]	±[b]
DG03	Quartz-molybdenite vein	27	2.6	0.01	1.7	0.01	3.2	0.02	117.5	0.8	0.9
FDG08	Quartz-polymetallic sulfide vein	20	7.1	0.03	4.4	0.02	8.6	0.03	116.4	0.6	0.7

Note: [a] analytical uncertainty, [b] analytical and decay constant uncertainty.

Table 2 $^{40}Ar/^{39}Ar$ analytical results of the ore-related sericite from the Sanyuangou deposit

T (°C)	$^{40}Ar/^{39}Ar$	$^{36}Ar/^{39}Ar$	$^{37}Ar/^{39}Ar$	$^{38}Ar/^{39}Ar$	$^{40}Ar^{*}$(%)	$^{40}Ar^{*}/^{39}Ar_{K}$	$^{39}Ar_{K}$ ($\times10^{-14}$mol)	$^{39}Ar_{Cumulative}$ (%)	Age (Ma)	± 1σ (Ma)
Sample SY02, J value = 0.004606, Total age = 115.1 Ma										
600	137.919	0.443	0.000	0.103	5.03	6.931	0.05	0.21	57	10
700	31.308	0.064	0.129	0.027	39.51	12.371	0.23	1.28	100	1.8
800	30.214	0.053	0.000	0.022	48.44	14.636	1.57	8.42	117.7	1.2
850	15.851	0.005	0.000	0.013	90.53	14.351	0.58	11.67	115.5	1.1
900	14.868	0.001	0.007	0.013	97.12	14.441	1.29	16.94	116.1	1.1
950	14.569	0.001	0.007	0.013	98.76	14.388	1.91	25.63	115.6	1.1
1000	14.866	0.001	0.032	0.013	97.22	14.453	11.72	79.05	116.3	1.1
1050	14.760	0.001	0.067	0.013	97.52	14.395	2.27	89.41	115.8	1.1
1150	15.173	0.003	0.383	0.014	93.62	14.210	0.99	93.93	114.4	1.2
1250	22.021	0.028	0.051	0.018	62.07	13.669	1.02	98.58	110.1	1.2
1400	147.832	0.047	0.000	0.099	6.88	10.164	0.31	100	82.5	2.3

Note: the terms $^{40}Ar^{*}$ and $^{39}Ar_{K}$ denote radiogenic ^{40}Ar and necleogenic ^{39}Ar, respectively.

Table 3 In-situ lead isotopic data for pyrite from Donggou and Sanyuangou

Deposit	Sample no.	Pb^{208}/Pb^{206}	2 σ	Pb^{207}/Pb^{206}	2 σ	Pb^{208}/Pb^{204}	2 σ	Pb^{207}/Pb^{204}	2 σ	Pb^{206}/Pb^{204}	2 σ	$^{205}Tl/^{203}Tl$	2 σ	Total Pb	Total Tl
Donggou	FDG09-1	2.198	0.0002	0.890	0.0001	38.147	0.009	15.445	0.003	17.357	0.002	2.425	0.00009	30.08	2.58
	FDG09-2	2.198	0.0001	0.890	0.0001	38.164	0.006	15.447	0.003	17.361	0.002	2.425	0.00009	37.13	2.59
	FDG09-3	2.198	0.0014	0.889	0.0004	38.155	0.098	15.419	0.027	17.328	0.034	2.425	0.00008	15.30	2.60
	FDG10-1	2.198	0.0006	0.890	0.0004	38.140	0.087	15.427	0.036	17.332	0.039	2.426	0.00009	1.79	2.76
	FDG10-2	2.199	0.0005	0.889	0.0002	38.243	0.067	15.452	0.022	17.385	0.022	2.426	0.00011	0.95	2.77
	FDG10-3	2.198	0.0004	0.890	0.0003	38.426	0.089	15.551	0.038	17.471	0.038	2.426	0.00010	0.54	2.75
	FDG10-4	2.199	0.0002	0.889	0.0002	38.118	0.039	15.408	0.014	17.335	0.016	2.426	0.00010	8.16	2.72
	FDG11-1	2.189	0.0071	0.890	0.0008	38.396	0.196	15.550	0.052	17.489	0.046	2.426	0.00010	0.62	2.60
	FDG11-2	2.196	0.0011	0.891	0.0006	38.080	0.168	15.439	0.069	17.336	0.085	2.426	0.00009	0.37	2.77
	FDG11-3	2.199	0.0008	0.888	0.0007	38.436	0.191	15.527	0.090	17.517	0.088	2.426	0.00010	7.12	2.73
	mean	2.197	0.0013	0.890	0.0004	38.230	0.095	15.466	0.035	17.391	0.037	2.426	0.00009	10.21	2.69
Sanyuangou	SY04-1	2.198	0.0002	0.892	0.0001	38.012	0.011	15.432	0.005	17.296	0.005	2.426	0.00010	11.49	2.71
	SY04-2	2.199	0.0001	0.893	0.0000	38.021	0.003	15.443	0.001	17.295	0.001	2.426	0.00010	37.55	2.73
	SY04-3	2.195	0.0012	0.890	0.0006	38.008	0.106	15.454	0.040	17.323	0.046	2.425	0.00009	0.48	2.73
	SY04-4	2.191	0.0012	0.888	0.0005	38.218	0.085	15.489	0.037	17.440	0.040	2.425	0.00007	0.48	2.76
	SY04-5	2.198	0.0009	0.889	0.0006	38.337	0.175	15.566	0.076	17.495	0.084	2.425	0.00009	0.26	2.66
	SY05-1	2.196	0.0005	0.892	0.0003	38.048	0.036	15.451	0.017	17.318	0.017	2.425	0.00009	6.23	2.69
	SY05-2	2.203	0.0003	0.894	0.0002	38.047	0.007	15.445	0.003	17.278	0.003	2.425	0.00008	27.78	2.66
	SY06-1	2.198	0.0002	0.893	0.0002	38.006	0.014	15.432	0.007	17.286	0.005	2.425	0.00009	17.19	2.71
	SY06-2	2.199	0.0002	0.893	0.0001	37.991	0.024	15.431	0.010	17.273	0.011	2.425	0.00012	1.45	2.73
	SY06-3	2.199	0.0001	0.893	0.0001	38.012	0.005	15.435	0.002	17.286	0.002	2.425	0.00010	55.60	2.75
	mean	2.198	0.0005	0.892	0.0003	38.070	0.047	15.458	0.020	17.329	0.021	2.425	0.00009	15.85	2.71

Appendix 1 Results of LA-ICP-MS zircon U-Pb dating for the Donggou granite porphyry, Sanyuangou quartz diorite, and Wangpingxigou quartz monzonite

Spot	Th	U	Th/U	Isotope ratio						Ag (Ma)					
				$^{207}Pb/^{206}Pb$	± 1σ	$^{207}Pb/^{235}U$	± 1σ	$^{206}Pb/^{238}U$	± 1σ	$^{207}Pb/^{206}Pb$	± 1σ	$^{207}Pb/^{235}U$	± 1σ	$^{206}Pb/^{238}U$	± 1σ
Donggou granite porphyry, sample DG01															
DG01-1	389	381	1.02	0.0490	0.0029	0.1236	0.0071	0.0184	0.0003	150	58	118	6	118	2
DG01-2	247	385	0.64	0.0496	0.0030	0.1238	0.0069	0.0184	0.0002	176	147	119	6	118	2
DG01-3	1911	3722	0.51	0.0550	0.0012	0.1411	0.0033	0.0184	0.0002	413	50	134	3	118	1
DG01-4	279	302	0.92	0.0495	0.0032	0.1229	0.0074	0.0185	0.0003	172	150	118	7	118	2
DG01-5	177	417	0.43	0.0488	0.0023	0.1239	0.0058	0.0185	0.0002	200	118	119	5	118	1
DG01-6	296	335	0.88	0.0501	0.0039	0.1253	0.0097	0.0184	0.0003	211	181	120	9	118	2
DG01-7	389	379	1.03	0.0491	0.0025	0.1232	0.0060	0.0184	0.0002	154	150	118	5	118	2
DG01-8	411	437	0.94	0.0513	0.0033	0.1289	0.0087	0.0185	0.0003	254	148	123	8	118	2
DG01-9	801	693	1.16	0.0485	0.0017	0.1240	0.0045	0.0185	0.0002	124	83	119	4	118	1
DG01-10	1026	600	1.71	0.0500	0.0033	0.1281	0.0086	0.0184	0.0002	195	156	122	8	118	1
DG01-11	320	279	1.15	0.0507	0.0044	0.1254	0.0107	0.0185	0.0004	228	204	120	10	118	3
DG01-12	311	360	0.87	0.0498	0.0031	0.1234	0.0074	0.0185	0.0003	187	146	118	7	118	2
DG01-13	457	539	0.85	0.0589	0.0035	0.1440	0.0076	0.0184	0.0003	561	127	137	7	117	2
Sanyuangou quartz diorite, sample SY01															
SY01-1	2403	1350	1.78	0.1085	0.0016	4.7579	0.0842	0.3168	0.0041	1776	27	1778	15	1774	20
SY01-2	1058	739	1.43	0.1096	0.0013	4.8453	0.0646	0.3187	0.0021	1794	22	1793	11	1783	10
SY01-3	997	739	1.35	0.1078	0.0013	4.6202	0.0592	0.3093	0.0019	1762	22	1753	11	1737	10
SY01-4	531	393	1.35	0.1075	0.0011	4.6456	0.0577	0.312	0.0024	1767	19	1758	10	1750	12
SY01-5	701	544	1.29	0.1079	0.0008	4.6809	0.0437	0.3129	0.0017	1765	13	1764	8	1755	8
SY01-6	1362	761	1.79	0.1071	0.0007	4.6555	0.0382	0.3131	0.0012	1751	13	1759	7	1756	6
SY01-7	1224	815	1.50	0.1069	0.0007	4.6203	0.0378	0.3113	0.0019	1748	11	1753	7	1747	9
SY01-8	358	518	0.69	0.1062	0.001	4.6717	0.0699	0.3165	0.0038	1735	17	1762	13	1772	18
SY01-9	987	835	1.18	0.1062	0.0006	4.6689	0.0355	0.3163	0.0017	1735	10	1762	6	1772	9
SY01-10	1275	942	1.35	0.1068	0.0007	4.7115	0.0436	0.3173	0.0017	1746	21	1769	8	1776	9
SY01-11	450	419	1.07	0.1086	0.0011	4.7737	0.0613	0.3167	0.0025	1776	14	1780	11	1774	12
SY01-12	491	481	1.02	0.1077	0.0012	4.7042	0.0645	0.3149	0.0024	1761	21	1768	11	1765	12
SY01-13	1149	889	1.29	0.1084	0.0014	4.8193	0.0706	0.3211	0.0025	1773	24	1788	12	1795	12
SY01-14	650	612	1.06	0.1074	0.0017	4.6636	0.0745	0.3141	0.0022	1767	28	1761	13	1761	11
Wanpingxigou quartz monzonite, sample WP01															
WP01-1	993	885	1.12	0.1118	0.0017	5.0921	0.0813	0.3282	0.0023	1829	23	1835	14	1830	11
WP01-2	343	324	1.06	0.1119	0.0019	5.0678	0.0838	0.3272	0.0027	1831	25	1831	14	1825	13
WP01-3	251	214	1.17	0.1166	0.0019	5.3102	0.0992	0.3282	0.0027	1905	34	1871	16	1830	13
WP01-4	433	397	1.09	0.1118	0.0014	5.05	0.0627	0.3265	0.0018	1829	23	1828	11	1821	9
WP01-5	738	592	1.25	0.1134	0.0008	5.1546	0.0536	0.3283	0.0023	1855	45	1845	9	1830	11
WP01-6	195	221	0.88	0.1141	0.0012	5.1774	0.0668	0.3276	0.0021	1865	19	1849	11	1827	10
WP01-7	712	618	1.15	0.1137	0.001	5.1542	0.0478	0.3272	0.0015	1859	17	1845	8	1825	7
WP01-8	467	400	1.17	0.1116	0.0017	5.0022	0.0736	0.3231	0.0023	1826	28	1820	12	1805	11
WP01-9	455	419	1.09	0.1127	0.0009	5.1369	0.0475	0.3278	0.0017	1844	15	1842	8	1828	8
WP01-10	167	258	0.65	0.1103	0.0016	4.9928	0.0706	0.3257	0.0026	1806	27	1818	12	1817	13
WP01-11	426	420	1.01	0.1102	0.0012	4.9717	0.0587	0.324	0.0016	1802	19	1815	10	1809	8
WP01-12	279	308	0.91	0.1114	0.0013	5.0624	0.0631	0.3264	0.0018	1822	16	1830	11	1821	9
WP01-13	203	285	0.71	0.1119	0.0023	5.0896	0.1138	0.3269	0.0035	1831	69	1834	19	1823	17
WP01-14	660	447	1.48	0.1122	0.0017	5.1388	0.0805	0.3293	0.0025	1836	27	1843	13	1835	12
WP01-15	801	585	1.37	0.1112	0.0020	5.0850	0.0900	0.3287	0.0019	1820	32	1834	15	1832	9

Appendix 2 LA-ICP-MS spot analytical data for pyrite from Donggou and Sanyuangou

Deposit	Sample no.	Analysis no.	Cr	Mn	Fe*	Co	Ni	Cu	Zn	Ga	As	Se	Mo	Ag	Cd	Sn	Sb	Te	Ba	Gd	Hf	Ta	W	Pt	Au	Tl	Pb	Bi
Donggou	FDG09-2-1	AU01A005	<4.89	38.23	460000	81.64	70.12	106.75	3007.69	0.31	251.35	2.94	22.36	55.55	22.26	6.00	31.22	4.91	0.21	<0.03	0.02	<0.01	0.28	<0.02	0.32	0.21	398.04	29.80
	FDG09-2-2	AU01A006	<2.49	180.38	460000	6.39	8.77	1942.29	494.63	0.19	44.66	1.94	<0.04	10.27	2.52	1.65	1.67	1.38	1.67	<0.01	<0.01	<0.01	<0.01	<0.01	<0.01	0.52	108.25	2.94
	FDG09-2-3	AU01A007	<3.10	2.60	460000	7.03	6.40	67.28	24.78	<0.02	8.54	2.93	0.06	0.87	0.19	0.20	0.72	0.37	<0.06	0.02	<0.02	<0.01	<0.01	<0.01	<0.01	0.02	23.72	1.06
	FDG09-3-4	AU01A008	<2.90	14.45	460000	20.21	4.68	13.19	809.68	<0.02	4.36	2.09	154.29	1.57	5.43	0.16	1.29	1.56	<0.07	<0.01	0.02	<0.01	0.10	<0.01	0.06	0.09	36.62	4.76
	FDG09-3-5	AU01A009	<3.05	<0.11	460000	6.72	0.14	3.08	0.31	<0.02	1821.40	1.16	<0.02	0.09	<0.07	0.12	0.94	0.82	<0.03	<0.04	<0.01	<0.01	<0.01	<0.01	0.20	<0.01	53.78	2.78
	FDG09-4-6	AU01A010	<2.75	0.21	460000	25.15	10.44	15.77	37.44	<0.01	4.39	1.43	<0.01	0.20	0.20	0.11	1.02	0.08	0.03	0.02	<0.01	<0.01	<0.01	<0.02	<0.01	0.01	7.30	0.06
	FDG09-4-7	AU01A011	<2.94	10.40	460000	1.17	0.08	1.47	0.49	<0.02	5.48	2.54	<0.01	0.41	<0.08	0.11	0.09	0.35	<0.05	<0.01	<0.01	<0.01	<0.01	<0.01	0.01	0.01	8.37	0.03
	FDG09-4-8	AU01A012	<3.50	<0.15	460000	1.49	0.33	1.79	0.65	<0.02	3.74	2.33	<0.04	0.17	<0.10	0.14	0.16	0.60	<0.04	0.01	<0.02	<0.01	<0.02	<0.02	0.03	<0.01	3.83	0.03
	FDG09-4-9	AU01A013	<2.57	0.81	460000	2.34	1.40	6.41	0.47	<0.01	17.32	2.01	<0.01	0.52	<0.05	0.12	0.57	1.27	0.04	<0.01	<0.01	<0.01	<0.01	<0.01	0.04	0.02	10.38	0.30
	FDG09-4-10	AU01A014	<4.54	78.99	460000	4.56	5.11	271.54	7512.98	<0.03	113.81	1.80	0.13	3.12	49.72	1.31	0.58	9.73	<0.06	<0.01	<0.04	<0.01	<0.02	<0.02	<0.01	0.01	23.34	0.41
	FDG11-1-1	AU01A015	<3.62	<0.10	459000	0.94	0.19	6.63	78.28	0.05	1362.45	2.49	0.05	3.50	0.35	0.10	0.19	<0.07	<0.06	<0.01	<0.02	<0.01	<0.01	<0.01	0.15	0.00	39.12	0.01
	FDG11-1-2	AU01A016	<2.82	<0.11	459000	0.14	0.10	0.16	0.35	<0.02	390.22	2.06	<0.03	<0.02	<0.05	0.10	<0.01	<0.13	<0.01	<0.03	<0.01	<0.01	<0.01	<0.01	<0.01	<0.01	0.07	<0.01
	FDG11-3-3	AU01A017	<3.73	<0.15	459000	3.12	1.52	0.84	0.32	<0.02	1.76	2.05	0.03	0.05	<0.05	0.12	0.07	0.46	0.07	<0.04	0.94	<0.01	<0.01	<0.02	<0.01	<0.01	2.28	0.20
	FDG11-3-4	AU01A018	<3.10	<0.12	459000	24.89	11.93	4.59	0.32	<0.02	94.31	2.51	0.03	0.33	<0.07	0.11	0.62	1.48	<0.01	<0.01	<0.01	<0.01	<0.01	<0.01	<0.01	0.01	7.27	1.00
	FDG11-3-5	AU01A019	<3.80	1.67	459000	491.57	115.34	1.73	<0.31	<0.02	37.90	2.14	0.30	0.03	<0.14	0.18	0.32	3.13	<0.08	<0.04	<0.02	<0.01	<0.02	<0.02	<0.01	0.01	11.65	1.20
	FDG11-3-6	AU01A020	<2.54	<0.11	459000	55.37	12.99	0.40	0.39	<0.02	1.84	2.63	<0.02	<0.01	<0.06	0.10	0.02	<0.17	<0.03	<0.01	<0.01	<0.01	<0.01	<0.01	0.01	<0.01	0.89	0.43
	FDG11-4-7	AU01A021	27.20	25.43	459000	180.72	23.06	3.76	3.49	2.65	74.88	6.05	0.44	1.30	<0.11	0.68	0.63	2.65	2.83	18.39	<0.01	<0.01	0.51	<0.02	<0.02	0.39	133.21	4.10
	FDG11-4-8	AU01A022	7.74	118.06	459000	112.44	22.38	8.78	15.96	5.79	53.62	1.95	1.76	2.38	<0.13	1.72	2.71	3.62	12.13	0.48	0.02	<0.01	0.35	<0.02	<0.01	1.55	156.19	2.77
	FDG11-4-9	AU01A023	<2.73	3.84	459000	61.63	36.62	2.25	1.04	0.38	136.08	1.59	<0.02	0.31	<0.06	0.23	2.22	0.48	1.53	<0.02	<0.01	<0.01	0.07	<0.01	<0.01	0.49	25.63	1.63
	FDG11-4-10	AU01A024	<2.97	9.71	459000	1224.09	116.10	2.93	<0.45	0.27	49.95	8.86	<0.05	1.63	<0.09	1.77	0.20	0.30	0.85	1.26	0.05	0.09	0.05	<0.02	0.16	<0.01	10.86	5.77
Sanyuangou	SY04-1-1	AU01A025	<2.06	<0.08	454000	3.05	1.13	7.36	0.63	<0.02	17213.55	1.47	<0.01	0.05	<0.04	0.09	<0.01	<0.12	<0.01	<0.01	<0.01	<0.01	<0.01	<0.01	11.96	<0.01	0.26	<0.01
	SY04-1-2	AU01A026	<2.82	<0.10	454000	5.84	0.29	4.25	0.29	<0.01	4916.60	2.17	<0.03	0.10	<0.05	0.11	<0.02	<0.08	<0.03	<0.01	<0.01	0.00	<0.01	<0.01	0.58	<0.01	0.05	<0.01
	SY04-1-3	AU01A027	<2.55	<0.08	454000	382.93	14.25	2.90	0.25	<0.02	7337.75	2.36	<0.03	<0.02	<0.07	0.12	<0.02	<0.10	<0.03	<0.03	<0.01	<0.01	<0.01	<0.01	4.63	<0.01	0.12	0.01
	SY04-2-4	AU01A028	<2.70	<0.13	454000	1289.78	34.08	475.78	0.54	<0.02	2928.28	2.25	<0.01	5.19	<0.08	0.13	0.14	<0.14	<0.07	0.03	<0.01	<0.01	<0.01	<0.01	0.44	<0.01	8.64	0.01
	SY04-2-5	AU01A029	<2.54	<0.08	454000	121.18	1.48	2.73	0.20	<0.02	9937.71	2.11	<0.01	0.02	<0.08	0.14	<0.01	<0.10	<0.04	<0.01	<0.01	<0.01	<0.01	<0.01	21.96	<0.01	0.02	<0.01
	SY04-2-6	AU01A030	6.25	<0.09	454000	33.12	2.86	9.37	10.67	<0.02	13113.92	2.14	<0.02	0.27	0.07	0.10	1.79	<0.13	0.04	<0.02	<0.01	<0.01	<0.01	<0.02	8.46	<0.01	1.04	<0.01
	SY04-2-7	AU01A031	<2.51	<0.10	454000	1.64	0.26	1355.14	3.18	<0.01	4469.19	2.26	<0.02	8.62	<0.04	0.11	<0.01	<0.09	<0.03	<0.01	<0.01	<0.01	<0.01	<0.01	1.09	<0.01	2.50	<0.01
	SY04-2-8	AU01A032	<2.67	3.97	454000	3.37	2.53	185.19	840.75	0.05	7810.34	<1.31	<0.02	4.38	3.39	1.12	2.31	<0.14	<0.01	<0.03	<0.01	<0.01	<0.01	<0.02	12.18	<0.01	18.18	<0.01
	SY04-4-9	AU01A033	<2.78	0.51	454000	601.95	255.99	7939.22	1.39	<0.01	<0.30	<1.36	<0.03	1091.60	0.28	0.61	0.73	0.10	<0.01	<0.01	<0.02	<0.01	0.25	<0.01	<0.01	2.18	167.53	0.01
	SY04-4-10	AU01A034	<2.12	0.16	454000	636.78	300.24	6161.43	59.80	0.05	0.83	2.15	<0.01	205.95	1.22	5.50	7.49	0.11	<0.01	<0.02	<0.01	0.00	0.11	<0.01	<0.01	1.51	637.60	<0.01
	SY03-1-1	NO06A003	3.16	84.97	456000	30.66	37.47	2650.71	11.47	0.16	1102.18	1.56	<0.01	16.00	0.14	0.16	2.06	<0.12	<0.02	<0.02	0.01	0.00	0.14	<0.01	<0.01	0.04	34.31	<0.01
	SY03-1-2	NO06A004	<0.44	2.46	456000	62.20	74.73	11087.95	26893.67	0.04	229.96	1.94	<0.01	85.69	203.54	0.12	0.77	<0.13	<0.06	<0.04	<0.01	<0.01	<0.02	<0.01	<0.01	0.01	101.06	<0.01
	SY03-1-3	NO06A005	1.03	17.25	456000	55.29	55.72	12666.89	2051.15	0.04	136.12	0.90	0.02	68.54	17.99	0.12	0.56	<0.17	<0.07	<0.02	0.03	0.02	0.06	<0.01	<0.01	0.01	43.08	<0.01
	SY03-1-4	NO06A006	<0.33	10.59	456000	64.37	4.41	11506.79	8944.66	<0.02	2955.85	1.72	<0.02	146.72	69.70	0.16	16.77	<0.17	<0.03	<0.02	0.02	<0.01	0.01	<0.01	0.05	0.07	234.89	0.03
	SY03-1-5	NO06A007	<0.47	<0.11	456000	38.62	60.01	9428.25	15250.56	<0.03	1071.85	1.51	<0.03	119.18	101.27	0.37	9.79	0.21	0.04	<0.02	<0.01	<0.01	<0.01	<0.01	0.02	0.03	176.81	0.01
	SY03-1-6	NO06A008	<0.33	2.04	456000	19.07	2.15	2588.46	4670.34	0.03	599.00	2.57	<0.02	47.50	38.23	0.17	7.37	<0.19	<0.03	<0.03	<0.01	0.00	<0.01	<0.01	<0.01	0.02	96.38	0.01
	SY03-1-7	NO06A009	<0.32	0.37	456000	75.41	61.23	2075.28	13.07	<0.02	106.77	0.77	<0.02	18.33	0.27	0.16	0.43	<0.14	<0.02	<0.01	0.00	<0.01	<0.01	<0.01	<0.01	<0.01	13.65	0.02
	SY03-1-8	NO06A010	3.13	302.27	456000	210.43	33.24	23420.20	9034.94	0.79	300.07	1.58	0.27	170.03	69.31	0.99	1.13	<0.16	0.39	<0.01	0.16	<0.01	0.05	<0.01	<0.01	0.03	179.43	0.02
	SY03-1-9	NO06A011	<0.37	7.26	456000	217.89	190.66	1752.82	35.07	<0.02	343.79	1.27	<0.02	15.57	0.17	0.11	1.10	<0.17	<0.05	<0.01	<0.01	<0.01	<0.01	<0.01	<0.01	0.01	53.49	<0.01
	SY03-1-10	NO06A012	<0.45	10.63	456000	26.74	7.01	4622.61	545.19	<0.03	1628.50	0.89	<0.01	50.72	6.88	0.13	0.24	<0.16	<0.02	<0.03	<0.01	<0.01	0.03	<0.01	<0.01	0.01	43.71	<0.01
	SY03-2-1	NO06A013	<0.38	1.67	456000	646.47	56.47	782.26	388.43	0.19	2658.79	1.63	<0.01	22.07	1.58	0.81	14.12	<0.15	0.37	<0.03	<0.01	0.00	<0.01	<0.01	1.81	0.01	154.17	<0.01
	SY03-2-2	NO06A014	3.09	6.27	456000	159.52	73.23	608.32	57.03	<0.04	1088.15	0.93	<0.02	4.96	0.23	0.64	1.68	0.14	0.63	0.03	0.93	<0.01	<0.01	<0.01	0.28	0.02	22.19	<0.01
	SY03-2-3	NO06A015	29.00	18.99	456000	2.19	2.68	4.57	3.10	0.41	3286.03	1.07	<0.02	1.34	<0.04	0.10	1.51	<0.13	0.87	0.11	0.60	0.01	0.23	<0.01	0.07	0.05	34.25	<0.01
	SY03-2-4	NO06A016	8.13	5.25	456000	5.47	2.48	3.78	0.69	0.66	12418.22	1.84	0.06	0.70	0.09	0.34	0.95	0.18	4.73	0.07	0.25	0.27	0.19	<0.01	2.45	0.06	20.02	<0.01
	SY03-2-5	NO06A017	0.50	32.21	456000	0.47	1.15	1046.99	4513.82	0.69	4196.21	<0.61	<0.02	29.15	17.18	2.17	14.53	<0.18	<0.03	0.01	<0.01	<0.01	<0.01	<0.01	2.40	0.02	165.76	0.02
	SY03-2-6	NO06A018	<0.47	5.11	456000	29.48	8.56	295.84	455.71	0.06	11234.28	1.26	<0.01	5.42	1.56	0.27	2.74	<0.17	<0.04	0.01	<0.01	<0.01	<0.01	<0.01	3.38	<0.01	24.68	<0.01
	SY03-2-7	NO06A019	<0.32	<0.10	456000	10.54	0.71	29.50	0.31	<0.03	14624.10	<0.85	<0.01	0.19	<0.06	0.09	0.04	<0.12	<0.02	<0.02	<0.01	<0.01	<0.01	<0.01	15.39	<0.01	1.00	<0.01
	SY03-2-8	NO06A020	<0.46	0.43	456000	9.28	0.89	100.66	47.82	<0.04	13559.60	1.28	<0.03	2.17	0.20	0.17	0.82	<0.19	<0.05	<0.03	<0.01	<0.01	0.01	<0.01	12.20	<0.01	7.57	0.01
	SY03-2-9	NO06A021	1.85	2.96	456000	137.63	49.86	175.70	132.51	0.74	304.43	1.34	0.02	2.77	0.57	0.33	0.90	<0.24	13.18	0.02	<0.01	<0.01	0.03	<0.01	0.06	0.02	31.93	0.02
	SY03-2-10	NO06A022	0.74	<0.11	456000	496.69	52.89	3.00	2.71	<0.03	17913.81	1.75	<0.03	0.35	<0.06	0.11	0.69	<0.20	<0.04	<0.04	<0.01	<0.01	<0.01	<0.01	3.53	0.02	23.33	<0.01

Note: * Iron was used as the internal standard, and the Fe contents were determined by EMP analyses

Highlights:

1) New geochronological data indicate that the Donggou Mo deposit and the spatially associated Sanyuangou Pb-Zn-Ag veins formed contemporaneously in the early Cretaceous (117.5-115.9 Ma).

2) Trace element compositions and lead isotopes of pyrite by in-situ LA-ICP-MS analyses confirm a magmatic-hydrothermal origin for the Sanyuangou Pb-Zn-Ag deposit.

3) The Donggou and Sanyuangou deposits form a typical porphyry-related magmatic-hydrothermal system. This model has broad implications for further exploration of Mo and Pb-Zn-Ag resources in the area.